frontiers in Earth Science

ORIGINAL RESEARCH
published: 27 January 2021
doi: 10.3389/feart.2020.613126

Development of Deep-Sea Anoxia in Panthalassa During the Lopingian (Late Permian): Insights From Redox-Sensitive Elements and Multivariate Analysis

Tetsuji Onoue[1]*, *Katsuhito Soda*[2] and *Yukio Isozaki*[3]

[1]Department of Earth and Planetary Sciences, Kyushu University, Fukuoka, Japan, [2]Center for Advanced Marine Core Research, Kochi University, Nankoku, Japan, [3]Department of Earth Science and Astronomy, The University of Tokyo, Tokyo, Japan

The end-Permian mass extinction (EPME) was the most severe mass extinction event of the Phanerozoic, and was associated with the development of global oceanic anoxia. The intensification of ocean anoxia preceded the EPME, but the degree of intensity and timing of oceanic redox changes in the mid-Panthalassa Ocean remain debated. Here we present the results of geochemical and multivariate statistical analyses of a late Guadalupian to Lopingian (middle–late Permian) bedded chert succession from the Iwaidani section, Japan, which preserves pelagic deep-sea facies from the ocean floor to the lower flank of a mid-Panthalassan seamount. The entire section yields a low manganese-enrichment factor (Mn_{EF} <1), suggesting that suboxic conditions has appeared in the depositional environment already in the late Guadalupian. Enrichment factors of other redox-sensitive trace-elements (e.g., vanadium and uranium) and principle component analysis (PCA) of major element data show the development of suboxic to weakly anoxic conditions across the Guadalupian/Lopingian boundary. Subsequently, anoxic conditions, as inferred from enrichments in U, Mo, Ni, Cu, Zn, and Tl, were developed during the middle Lopingian. Extremely high concentrations of U and Mo (enrichment factors of ~6 and ~5,500, respectively) indicate that H_2S-rich euxinic conditions developed during the latest Lopingian and around the time of the EPME. The cause of the shift toward more reducing conditions in the early–middle Lopingian is unknown, but PCA results suggest that the euxinic conditions occurred in association with intensified continental weathering in response to a temperature rise during the ca. 200 kyr before the EPME.

Keywords: Mino Belt, chert, principal compoment analysis, chemical weathering, anoxia, Permian/Triassic boundary

OPEN ACCESS

Edited by:
André Jasper, Universidade do Vale do Taquari—Univates, Brazil

Reviewed by:
William J. Foster, Museum of Natural History Berlin (MfN), Germany
Changqun Cao, Nanjing Institute of Geology and Paleontology (CAS), China

***Correspondence:**
Tetsuji Onoue
onoue.tetsuji.464@m.kyushu-u.ac.jp

Specialty section:
This article was submitted to Paleontology, a section of the journal Frontiers in Earth Science

Received: *01 October 2020*
Accepted: *08 December 2020*
Published: *27 January 2021*

Citation:
Onoue T, Soda K and Isozaki Y (2021) Development of Deep-Sea Anoxia in Panthalassa During the Lopingian (Late Permian): Insights From Redox-Sensitive Elements and Multivariate Analysis. Front. Earth Sci. 8:613126. doi: 10.3389/feart.2020.613126

INTRODUCTION

The Permian/Triassic boundary (PTB) marks the most severe mass extinction of the Phanerozoic, characterized by the loss of ~80% of marine invertebrate species (e.g., Erwin, 1994; Payne and Clapham, 2012; Stanley, 2016). A high-precision age model from the PTB section in Meishan, China revealed that the end-Permian mass extinction (EPME) occurred just before the PTB at ca. 251.94 Ma (Burgess et al., 2014). Extinctions have been confirmed on the genus and family

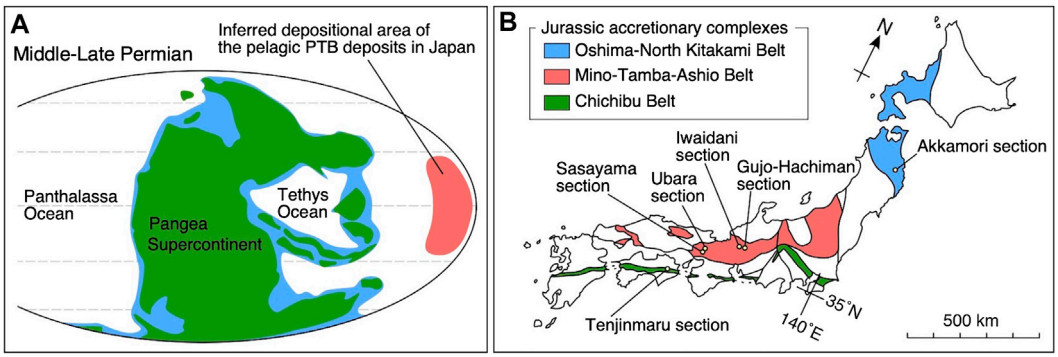

FIGURE 1 | (A) Middle–Late Permian paleogeographic map showing approximate location of the inferred depositional site of the pelagic Permian–Triassic deposits (bedded chert) of Japan in the Panthalassa Ocean. **(B)** Position of the Iwaidani section and previously studied Permian/Triassic boundary sections in Japan. The distribution of Jurassic accretionary belts of Japan is modified from Isozaki et al. (2010).

levels in age-diagnostic marine taxa such as fusulinids, ammonoids, conodonts, and radiolarians (Brayard et al., 2006, Brayard et al., 2009; Isozaki, 2009; Jiang et al., 2011; Chen and Benton, 2012; Feng and Algeo, 2014). The release of volcanic and contact metamorphic carbon and sulfur gases (CO_2, CH_4, and SO_2) from the Siberian Traps is commonly invoked as the trigger for climatic perturbations across the PTB (e.g., Wignall 2007; Burgess et al., 2017), which led to the EPME. Numerous lines of evidence from the low-latitude Paleotethys and high-latitude Boreal oceans indicate that hydrogen sulfide (H_2S)-rich euxinic conditions developed around the time of the EPME (Cao et al., 2009; Schobben et al., 2015; Lau et al., 2016; Zhang et al., 2017; Zhang et al., 2018b, Zhang et al., 2020).

In the Panthalassa Ocean, widespread deep-water anoxic conditions are thought to have occurred during the late Guadalupian (late middle Permian) to Early Triassic. Isozaki, 1994, Isozaki, 1997) was the first to demonstrate the existence of prolonged anoxia ("deep-sea anoxia") starting as early as ca. 7 myr prior to the PTB, on the basis of lithostratigraphic, petrographic, and mineralogical data from the PTB sections in Japan and western Canada. However, recent studies have argued against this hypothesis (Wignall et al., 2010; Fujisaki et al., 2019). For example, the contents of redox-sensitive trace-metals (e.g., U, Mo, and V) and quantitative analysis of framboidal pyrite size distribution from a PTB section at Gujo-Hachiman in Japan (**Figure 1**) show that the Lopingian deep-sea was dominated by oxic conditions, but that the oxygen minimum zone (OMZ) rapidly expanded at shallower depths in the mid-Panthalassa immediately before the EPME (Algeo et al., 2010, 2011b; Wignall et al., 2010; Fujisaki et al., 2019). Uranium isotopic studies of shallow-water carbonates from the Tethyan and Panthalassic oceans also suggest that the global marine redox conditions during the Guadalupian and Lopingian (late Permian) were similar to those of the modern ocean, and that a major expansion of oceanic anoxia began ≤70 kyr before the EPME (Brennecka et al., 2011; Elrick et al., 2017; Zhang et al., 2018a; Zhang et al., 2020). Thus, the duration and intensity of the EPME-related deep-sea anoxia remain debated.

The PTB sections of the Mino Belt, central Japan (**Figure 1**) preserve high-resolution biostratigraphic records of the EPME in a mid-oceanic realm of the Panthalassa Ocean (Kuwahara et al., 1998; Yao et al., 2001; Sano et al., 2010; Nishikane et al., 2011; Sano et al., 2012a; Sano et al., 2012b; Nishikane et al., 2014; Kuwahara and Sano, 2017). The intensification of oxygen-depleted conditions during the latest Lopingian has been reported from several PTB sections in the Mino Belt (Wignall et al., 2010; Algeo et al., 2011b; Sano et al., 2012b; Onoue et al., 2019). An improved understanding of the oceanic redox conditions during the Guadalupian and Lopingian (Kato et al., 2002; Kakuwa, 2008; Kato and Isozaki, 2009; Fujisaki et al., 2019) is central to understanding the link between global-ocean conditions and the EPME, as well as the subsequent delayed biotic recovery during the Early Triassic.

To better understand the redox history of the deep-sea Panthalassa Ocean during the Guadalupian and Lopingian, this paper describes variations in the contents of redox-sensitive elements (e.g., Mn, V, Mo, U) in a Capitanian (upper Guadalupian) to Induan (Lower Triassic) bedded chert succession from the Iwaidani section, Japan (Sano et al., 2012a; Kuwahara and Sano, 2017). We also applied principal component analysis (PCA) to major element contents to investigate the environmental conditions that triggered the changes in oceanic redox conditions. The Permian bedded cherts in the Mino Belt were originally composed of biogenic silica and carbonate, terrigenous detrital material transported as aeolian dust from the continent, and hydrogenous materials such as Fe–Mn oxides. The PCA results enable us to separate the signals from these multiple source materials, and indicate enhanced continental weathering accompanied by a change from anoxic to euxinic conditions in the Panthalassa Ocean.

GEOLOGICAL SETTING AND STUDIED SECTION

We examined PTB siliceous rocks of the Mino Belt in the Mt. Funabuseyama area, Japan, which is a Jurassic subduction-related

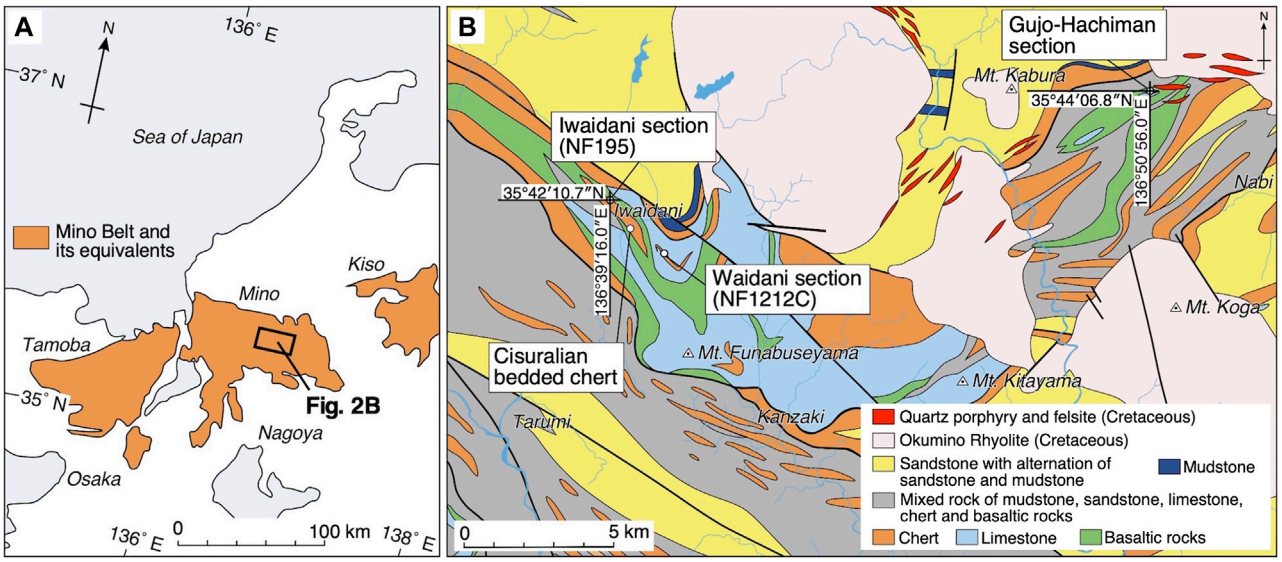

FIGURE 2 | (A) Location map of the study area in the Mino Belt, central Japan. **(B)** Geologic map of the Mt. Funabuseyama area (after Sano, 1988a; Wakita, 1988; Wakita et al., 1992). Map showing the locations of the Iwaidani section, including the Cisuralian red chert (Sano, 1988a; Sugitani et al., 1991), and other pelagic Permian/Triassic boundary sections in the area.

accretionary complex (**Figure 2**). The Mino Belt in the study area consists of mixed rock assemblages in which numerous blocks and lenses of various lithologies (e.g., basalt, limestone, and bedded chert) and size are mingled with terrigenous clastic rocks (Wakita, 1988; Sano et al., 1992). Basaltic rocks, limestone, and bedded chert of the Mino Belt form a Permian oceanic-rock assemblage, devoid of terrestrial detritus. Sano (1988a) divided the Permian oceanic-rock assemblage in the Mt. Funabuseyama area into three successions nearly in time-equivalent stratigraphy: 1) upper Cisuralian (upper lower Permian) to upper Guadalupian shallow-marine limestone, 2) upper Cisuralian carbonate breccia, and 3) middle Cisuralian to upper Lopingian bedded chert with the overlying Lower Triassic black claystone, all of which are underlain by basaltic rocks (Sano, 1988a; Sano, 1988b; Sano, 1989). The former two successions are interpreted to have accumulated on and around an oceanic seamount in the mid-Panthalassa Ocean (Sano et al., 1992; Jones et al., 1993; Safonova et al., 2016). The Permian bedded chert-dominated succession was part of the Hashikadani Formation (Sano, 1988a), and was interpreted to comprise pelagic facies deposited on the deep-ocean floor and on the lower flank of a mid-Panthalassa seamount (Sano, 1988a; Sano et al., 2010). The bedded cherts of the Hashikadani Formation lack coarse terrigenous grains, suggesting that their primary depositional site was beyond the reach of land-derived clastic material, in the pelagic realm of the Panthalassa Ocean (Sano et al., 2010).

The rocks examined in the present study correspond to the Permian–Lower Triassic Hashikadani Formation, and crop out along a roadcut near Iwaidani in the Mt. Funabuseyama area (Sano et al., 2012a). In previous studies, the section was referred to as NF195 (Sano et al., 2012a; Kuwahara and Sano, 2017); in this study, we call it the Iwaidani section. This section comprises six subsections (NF195A–NF195F; Sano et al., 2012a; Kuwahara and Sano, 2017) along a 30 m-long roadcut outcrop. There is a possible depositional gap between the NF195B and NF195C subsections, as evidenced by a minor fault (Kuwahara and Sano, 2017). Sano et al. (2012a) and Kuwahara and Sano (2017) explored individual beds in the sections and confirmed that the remainder of the subsections are stratigraphically continuous.

The **Figure 3** shows the composite litho-biostratigraphy of the Permian bedded chert to Lower Triassic black claystone sequence in the Iwaidani section. The section comprises a lower unit of gray bedded chert with small amounts of dark gray to black chert and black claystone, a middle unit of black bedded chert including pyrite nodules near the top, and an upper unit characterized by black claystone with thin black chert beds (Sano et al., 2012a). Biostratigraphic studies have assigned a Capitanian to Induan age to the entire Iwaidani section on the basis of radiolarian and conodont occurrences, such as *Follicucullus charveti*, *F. porectus*, *Albaillella yamakitai*, *A. triangularis*, *Neoalbaillella optima*, and *Hindeodus parvus* (**Figure 3**) (Sano et al., 2012a; Kuwahara and Sano, 2017). Based on the biostratigraphic ages from Nishikane et al. (2011), the first occurrence of *A. cavitata* can be correlated with the base of the Guadalupian–Lopingian transition zone (GLT) (Nishikane et al., 2011; Nishikane et al., 2014), which is also recognized in the Gujo-Hachiman section located ~18 km east of the Iwaidani section (**Figure 2B**). Kuwahara and Sano (2017) showed that lower Wuchiapingian radiolarian species, such as *A. protolevis* and *Neoalbaillella*? sp. firstly appear in the basal part of the *N. ornithoformis* assemblage zone. This result is consistent with the age assignment by Kuwahara et al. (1998) that correlated the *N. ornithoformis* assemblage zone with the lower Lopingian (**Figure 3**). Biostratigraphic analysis of radiolarians also revealed that the Iwaidani section contains the

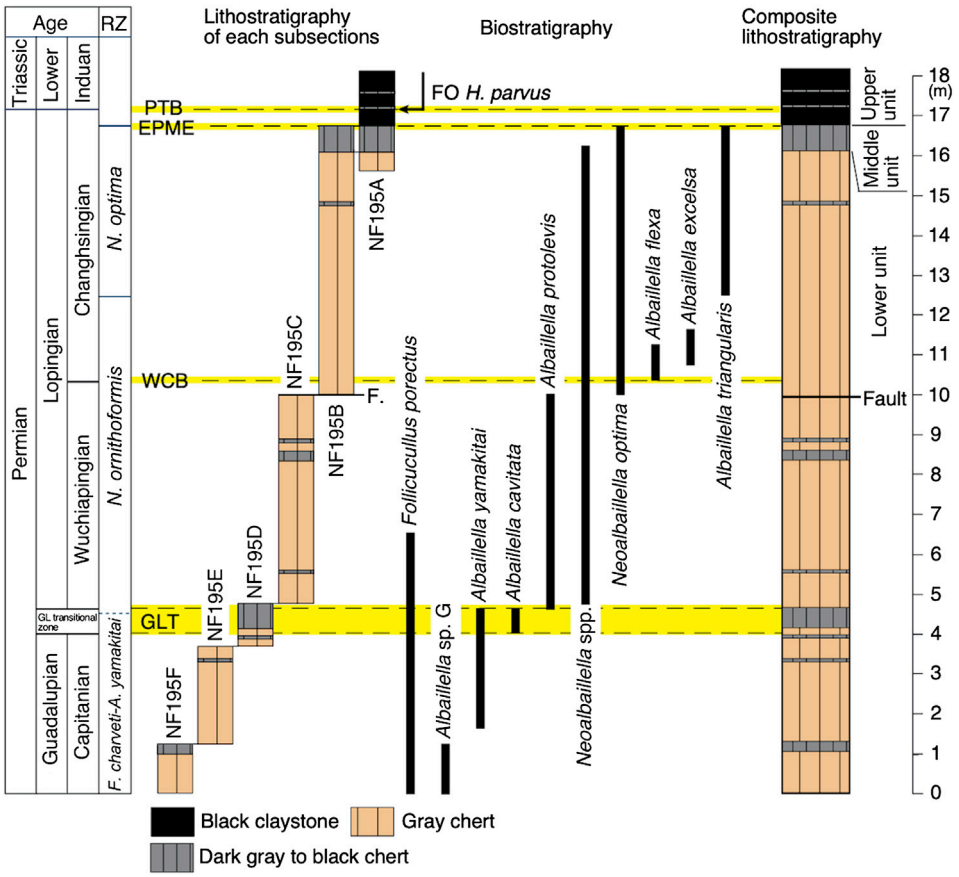

FIGURE 3 | Lithostratigraphy and radiolarian biostratigraphy of the Iwaidani section, after Sano et al. (2010) and Kuwahara and Sano (2017). PTB = Permian/Triassic boundary; EPME = end-Permian mass extinction; WCB = Wuchiapingian/Changhsingian boundary; GLT = Guadalupian–Lopingian transitional zone; RZ = radiolarian assemblage zone.

Wuchiapingian/Changhsingian boundary (WCB) in the basal ~10.3 m of the lower unit, based on the first occurrence of *A. flexa* (Sano et al., 2012a). The EPME horizon of Permian radiolarians occurs at the top of the middle unit (Sano et al., 2012a). The base of the Triassic is defined by the presence of the conodont *Hindeodus parvus* in the upper unit (Sano et al., 2012a).

METHODS

Sample Collection and Preparation

The studied Permian bedded chert consists of rhythmic successions in the form of chert and thin siliceous claystone beds. Previous sedimentological and geochemical studies have revealed that the chert beds are the SiO_2-diluted parts of siliceous claystone beds, as indicated by an increase in radiolarian tests (Hori et al., 1993; Takiguchi et al., 2006). The chert bed samples contain over 90% SiO_2, which results in the dilution of major oxides (TiO_2, MgO, CaO, Na_2O, K_2O, and P_2O_5) and trace elements by the large amount of biogenic silica. This SiO_2-dilution can enlarge the relative errors of compositional data, which affects the results of multivariate analysis (Soda and Onoue, 2019). Therefore, we focused on the geochemical compositions of the intercalated siliceous claystones.

We collected 114 claystone samples from the Iwaidani section for bulk-rock geochemical analysis. Each sample was crushed in an agate mortar to 5–10 mm in size and handpicked to avoid contamination from veins and intensely weathered material. These handpicked fragments were washed by ultrasonic cleaning in Milli-Q deionized water (>18 MΩ). After air-drying, the fragments were pulverized in an agate planetary mill for major and trace element analyses.

Major, Trace, and Rare Earth Element Analyses

Major element (Si, Ti, Al, Fe, Mn, Mg, Ca, Na, K, and P) and Ni, Cu, and Zn contents were determined with an energy dispersive X-ray fluorescence (XRF) spectrometer (PANalytical Epsilon 3^{XLE}) with a Mo X-ray tube at Kyushu University, Fukuoka, Japan. Analyses were calibrated using 20 standard rock samples issued by the Geological Survey of Japan. Detection limits for trace elements were 3 ppm for Ni and 2 ppm for Cu and Zn. Reproducibility based on the replicate analysis of two standards

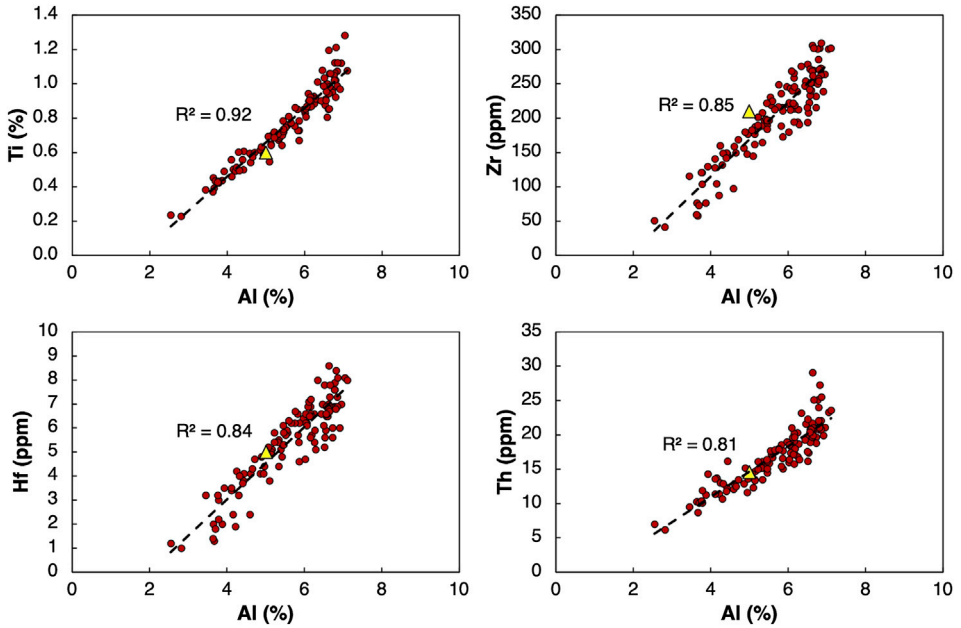

FIGURE 4 | Scatter plots of Al vs. Ti, Zr, Hf, and Th for the siliceous claystone samples. Ti/Al, Zr/Al, Hf/Al, and Th/Al ratios are the same as those of PAAS (yellow triangle) (Taylor and McLennan, 1985).

issued by Geological Survey of Japan (JSd-1 and JSd-3) was better than ± 1% for Al, Mn, Na, Ti, Ca, K, Ni, Cu, and Zn, and ± 4% for P.

Samples were analyzed for trace and rare Earth element (REE) concentrations using inductively coupled plasma–mass spectroscopy (ICP–MS) with lithium metaborate/tetraborate fusion at Actlabs (package Code 4B2-STD), Ancaster, Canada. Ten international rock and mineral standards were also analyzed for quality control during trace and REE analyses. For details of the analytical techniques, see www.actlabs.com.

Principal Component Analysis

To extract paleoenvironmental changes from the compositional data, principal component analysis (PCA) was applied to data for the ten major oxides (SiO_2, Al_2O_3, MgO, CaO, K_2O, TiO_2, Na_2O, P_2O_5, Fe_2O_3, and MnO). We limited PCA to major elements, because some trace elements had large analytical uncertainties and/or were below the detection limit (**Supplementary Table S1**). To use the major element contents for PCA, the data were normalized using Ti contents and compared with those of post-Archean average Australian shale (PAAS) (Taylor and McLennan, 1985) to obtain enrichment factors, defined as follows:

$$X_{EF} = \left(X_{sample}/Ti_{sample}\right)/\left(X_{PAAS}/Ti_{PAAS}\right)$$

where X and Ti are the weight contents of element X and Ti, respectively.

PCA is a multivariate statistical analysis that synthesizes numerous observational variables into several orthogonalized principal components (PCs) maximizing the respective variances. Before performing a Q-mode PCA on a correlation coefficient matrix using a singular value decomposition (Golub and Van Loan, 1989; Van Huffel and Vanderwalle, 1991; Albarède, 1995), the enrichment factors were converted into additive log ratios to map the simplex sample space onto the Euclidean real sample space for a constant sum (Aitchison, 1986). This is done because it transforms most of the compositional data into multivariate normal distributions (Aitchison and Shen, 1980; Reyment and Hirano, 1999), which is a prerequisite for PCA (e.g., Atkinson et al., 2004). Consequently, for elements that are less mobile during weathering and diagenesis, such as Ti, whose intermediate ionic potential leads to the formation of stable or metastable individual solids in the Earth surface environment (Stumm and Morgan, 1996; Langmuir, 1997; Railsback, 2007), PCA optimizes an otherwise cumbersome interpretation (Woronow and Love, 1990; Turner et al., 2003).

RESULTS

Major and Trace Elements

The major and trace element data obtained from the 114 siliceous claystone samples of the Iwaidani section are listed in **Supplementary Table S1**. In all of the samples, Al is positively correlated with Ti and high field strength (HFS) elements such as Zr, Hf, and Th (**Figure 4**). Since elements such as Al, Ti, Zr, Hf, and Th are not significantly mobilized during post-depositional processes, including diagenesis and weathering, these positive correlations indicate that most of these elements have a detrital origin; potassium (K) is also

	Si																												
Ti	-.92	Ti																											
Al	-.95	.96	Al																										
Fe	-.60	.38	.36	Fe																									
Mn	-.13	.07	.07	.19	Mn																								
Mg	-.64	.58	.56	.35	-.01	Mg																							
Ca	-.02	.02	.00	-.06	-.06	.36	Ca																						
Na	-.48	.53	.55	.33	.07	.04	-.27	Na																					
K	-.88	.91	.97	.20	.03	.52	.02	.50	K																				
P	-.37	.30	.24	.36	.05	.56	.63	-.16	.18	P																			
V	-.01	.15	.09	.02	.01	-.17	-.22	.45	.04	-.25	V																		
Cr	-.88	.90	.89	.45	.11	.49	-.05	.58	.80	.24	.22	Cr																	
Ni	-.41	.29	.25	.58	.56	.29	-.01	.25	.11	.34	.28	.30	Ni																
Cu	-.55	.49	.42	.67	.26	.14	-.14	.45	.30	.24	.21	.48	.58	Cu															
Zn	-.53	.43	.39	.64	.35	.49	.10	.17	.25	.54	.00	.45	.90	.57	Zn														
Rb	-.88	.89	.94	.24	.04	.56	.00	.43	.95	.26	-.03	.83	.14	.35	.32	Rb													
Sr	-.70	.78	.75	.32	.18	.40	-.03	.64	.72	.29	.26	.73	.37	.56	.43	.75	Sr												
Y	-.68	.76	.68	.26	.13	.51	.26	.21	.66	.54	-.05	.66	.23	.45	.43	.73	.69	Y											
Zr	-.90	.93	.92	.31	.05	.60	.01	.36	.91	.30	.00	.85	.17	.39	.35	.94	.71	.76	Zr										
Nb	-.92	.93	.93	.35	.05	.62	.02	.37	.90	.30	-.01	.87	.19	.41	.38	.94	.70	.75	.99	Nb									
Mo	-.13	-.11	-.08	.59	-.06	-.14	-.31	.10	-.07	-.07	-.23	-.08	-.18	.38	-.17	-.10	-.12	-.17	-.07	-.05	Mo								
Ba	-.41	.39	.45	-.16	-.03	.38	.25	-.22	.52	.18	-.34	.25	-.26	-.18	-.11	.49	.07	.39	.56	.54	-.18	Ba							
ΣREE	-.75	.85	.76	.32	.16	.49	.12	.39	.71	.48	.17	.78	.32	.51	.47	.76	.80	.91	.81	.79	-.18	.30	ΣREE						
Hf	-.91	.93	.92	.34	.06	.66	.09	.33	.89	.38	-.04	.85	.22	.40	.41	.93	.71	.79	.99	.98	-.07	.56	.82	Hf					
Ta	-.92	.96	.94	.37	.06	.62	.02	.43	.91	.31	.08	.90	.26	.44	.42	.93	.75	.75	.97	.98	-.07	.47	.83	.98	Ta				
Tl	-.11	.05	.06	.30	.84	-.12	-.15	.35	.00	-.06	.27	.17	.63	.28	.31	-.05	.19	-.05	-.07	-.06	.02	-.29	.07	-.07	-.01	Tl		
Th	-.86	.94	.90	.30	.04	.56	.01	.44	.87	.29	.21	.86	.21	.41	.35	.88	.76	.78	.95	.93	-.14	.46	.87	.94	.96	-.04	Th		
U	.17	-.07	-.13	.04	.05	-.26	-.20	.39	-.16	-.25	.73	-.08	.56	.25	-.02	-.25	.09	-.24	-.24	-.24	.00	-.48	-.07	-.25	-.15	.34	-.05		

0.70 ≤ r < 0.80 0.80 ≤ r < 0.90 0.90 ≤ r < 1.00

FIGURE 5 | Correlation coefficients between measured elemental contents in the siliceous claystone samples. ΣREE_{EF} represents the total REE concentrations.

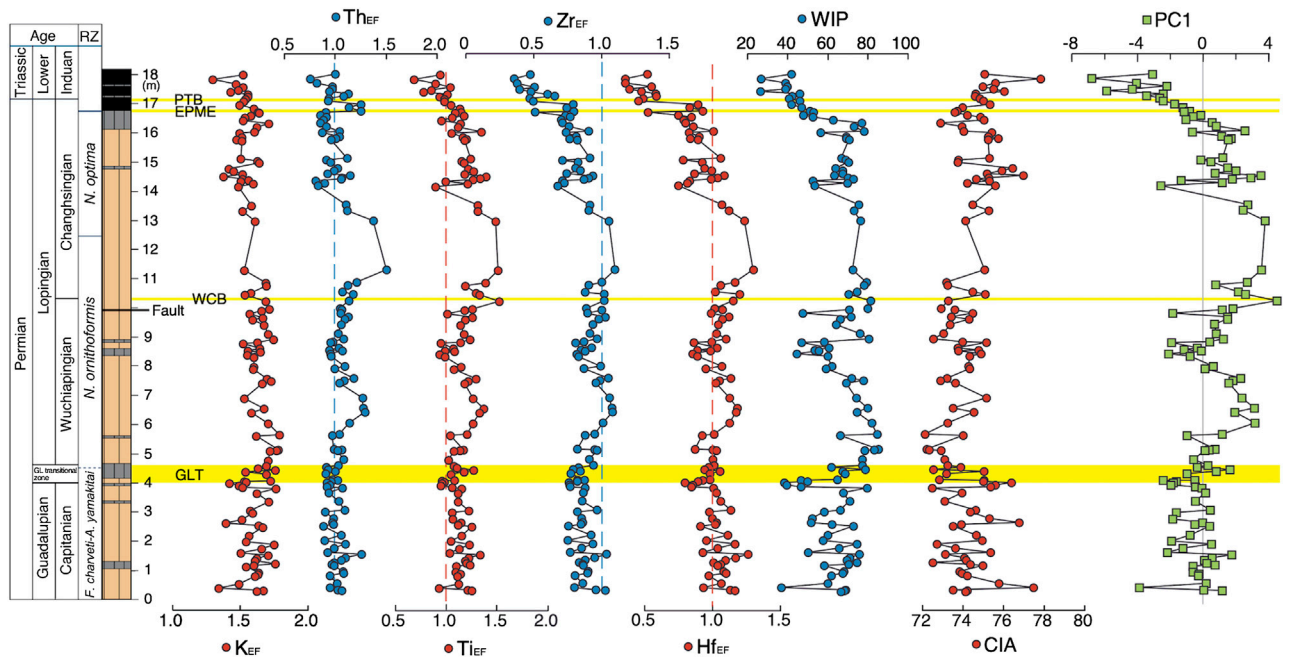

FIGURE 6 | Enrichment factors of elements in detrital materials (K, Th, Ti, Zr, and Hf), weathering indices (WIP and CIA), and PC1 scores plotted with stratigraphy. Enrichment factors (EF) were calculated relative to PAAS (Taylor and McLennan, 1985). Dashed blue and red lines indicate PAAS enrichment values of 1.

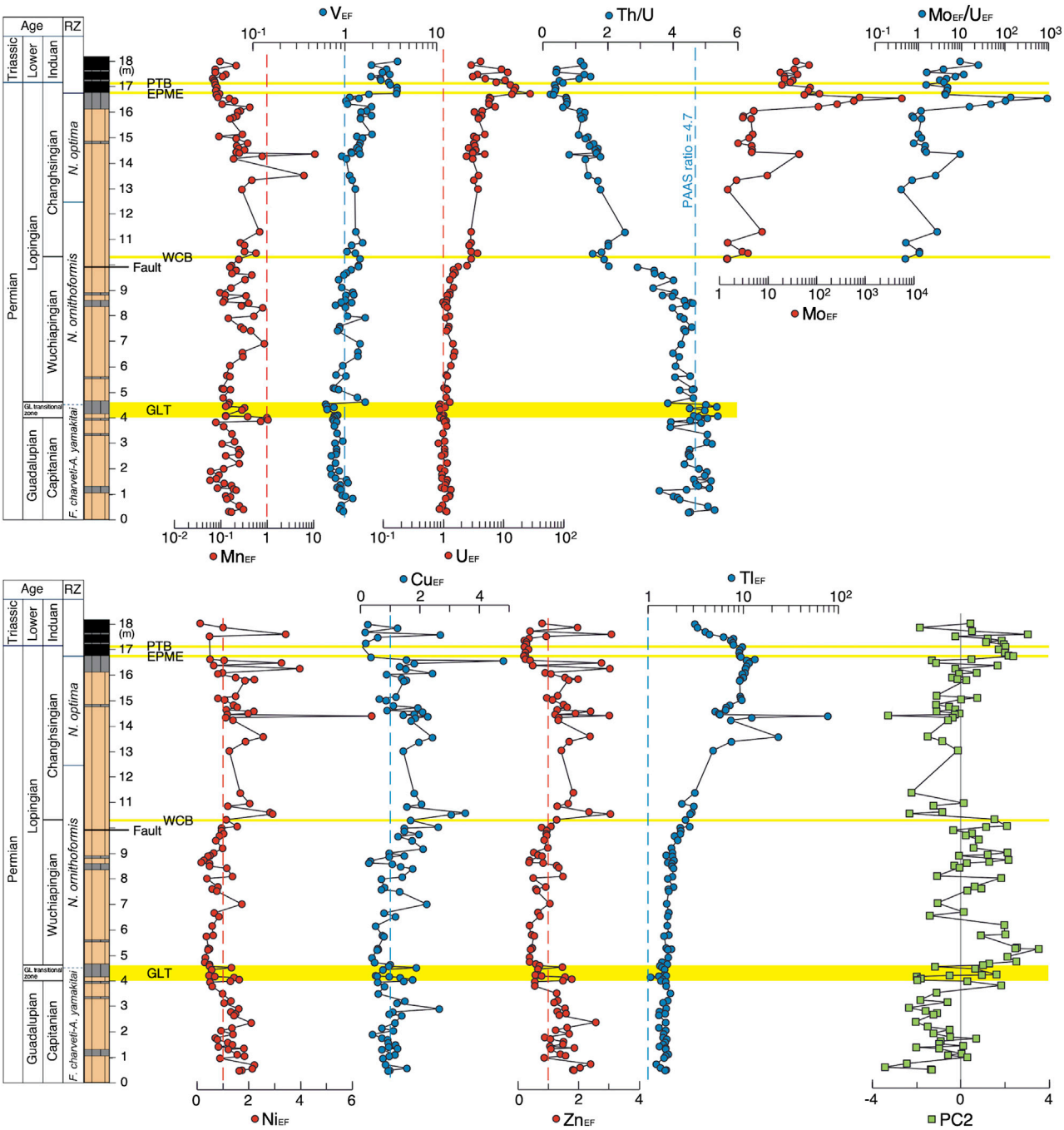

FIGURE 7 | Enrichment factors (EF) of redox-sensitive elements (Mn, V, U, Mo, Ni, Cu, Zn, and Tl), Th/U, Mo_{EF}/U_{EF}, and PC2 scores plotted with stratigraphy. EFs of Mn, V, U, Mo, Ni, Cu, and Zn were calculated relative to PAAS (Taylor and McLennan, 1985), and Tl was calculated relative to upper continental crust (UCC; McLennan, 2001).

correlated with the elements in detrital materials (**Figure 5**). The elemental ratios between these elements in our samples are indistinguishable from those of PAAS (**Figure 4**). Their similarity to average shale composition (Taylor and McLennan, 1985) indicates that the detrital materials in the Iwaidani section samples have a terrigenous origin, which is consistent with the geochemistry of the Permian–Triassic siliceous rocks at the Sasayama section in Japan (**Figure 1B**; Kato et al., 2002). Conversely, no correlations were found between these terrigenous elements and elements such as P,

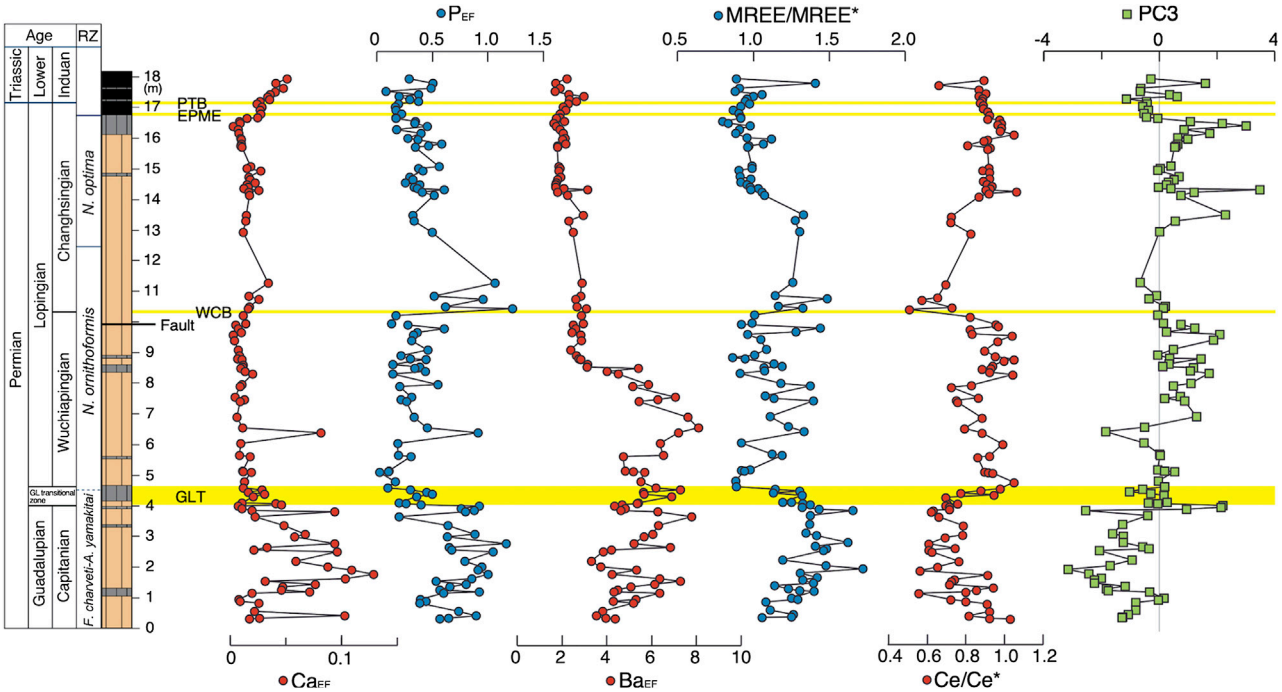

FIGURE 8 | Ca_{EF}, P_{EF}, Ba_{EF}, MREE/MREE*, Ce/Ce*, and PC3 score plotted with stratigraphy. Enrichment factors (EF) were calculated relative to PAAS (Taylor and McLennan, 1985).

Ba, Mn, V, U, and Mo (**Figure 5**), which are typically derived from biogenic and/or hydrogenous sources (Calvert and Pedersen, 2007).

To avoid the significant dilution effect by biogenic SiO_2, concentrations of the elements were normalized to Al concentrations and compared with those of the PAAS (Taylor and McLennan, 1985) to obtain enrichment factors. **Figure 6** shows the enrichment factors of K, Ti, Zr, Hf, and Th. Values of K_{EF} and Th_{EF} (1.59 ± 0.10 and 1.02 ± 0.12, respectively; average ± 1SD) are fairly constant throughout the studied section and close to the value of 1, where 1 represents the sample having the exact same ratio as PAAS. In the Capitanian and Wuchiapingian, the values of Ti_{EF}, Zr_{EF}, and Hf_{EF} are similar to those of PAAS; in the late Changhsingian the enrichment factors for these elements show a rapid decrease.

Enrichment factors for Mn, Ni, Cu, Zn, Tl, V, U, and Mo have been widely used to characterize the redox conditions of marine environment (e.g., Calvert and Pedersen, 1993; Calvert and Pedersen, 2007; Algeo and Tribovillard, 2009; Takahashi et al., 2014; Algeo and Li, 2020), which can be generally classified as oxic, dysoxic, suboxic, anoxic, or euxinic state (presence of free H_2S) (Tyson and Pearson, 1991). Enrichment factors of Mn, V, U, Mo, Ni, Cu, and Zn in **Figure 7** were calculated relative to PAAS (Taylor and McLennan, 1985), and Tl was calculated relative to upper continental crust (UCC; McLennan, 2001). In this study, the entire section exhibits a low enrichment factor for Mn (Mn_{EF} <1). Enrichment factors for V and U are generally close to the value of 1 during the Capitanian, but increase slightly across the GLT. Increases in Ni_{EF}, Cu_{EF}, Zn_{EF}, Tl_{EF}, and U_{EF} occur across the WCB. An increase in Mo_{EF} also occurs above the WCB. Vanadium, U, and Mo enrichment factors continued to increase during the latest Changhsingian. In particular, Mo_{EF} reached a peak of 5,000 (Mo content = 5,370 ppm).

Calcium, P, and Ba are widely used as proxies for the burial flux of biogenic material (Hollis et al., 2003; Takiguchi et al., 2006; Algeo et al., 2011b; Soda and Onoue, 2018; Soda and Onoue, 2019; Sato et al., 2020) based on their distribution and deposition in modern marine sediments (e.g., Schroeder et al., 1997). **Figure 8** shows changes in the enrichment factors against the stratigraphic frame in the present study. The trends in Ca_{EF} and P_{EF} decreased abruptly in the late Capitanian, and these elements are positively correlated with each other (r = 0.62; **Figure 9**). There is an abrupt decrease in Ba_{EF} during the Wuchiapingian, and Ba_{EF} remains relatively low during the Changhsingian.

Rare Earth Elements

Figure 10 shows the rare Earth element (REE) patterns of the Iwaidani section normalized to PAAS (Taylor and McLennan, 1985). The REE patterns of the Guadalupian samples are moderately to highly enriched in middle REEs (MREE: Sm, Gd, Tb, and Dy), whereas most of the Lopingian samples yield rock/PAAS ratios of 1. The REE ratios for the Lower Triassic claystones are relatively flat and lower than 1. Since the enrichment of the MREEs exhibits stratigraphic changes, we calculate the relative MREE enrichments using PAAS-normalized MREE/MREE* ratios (Chen et al., 2015):

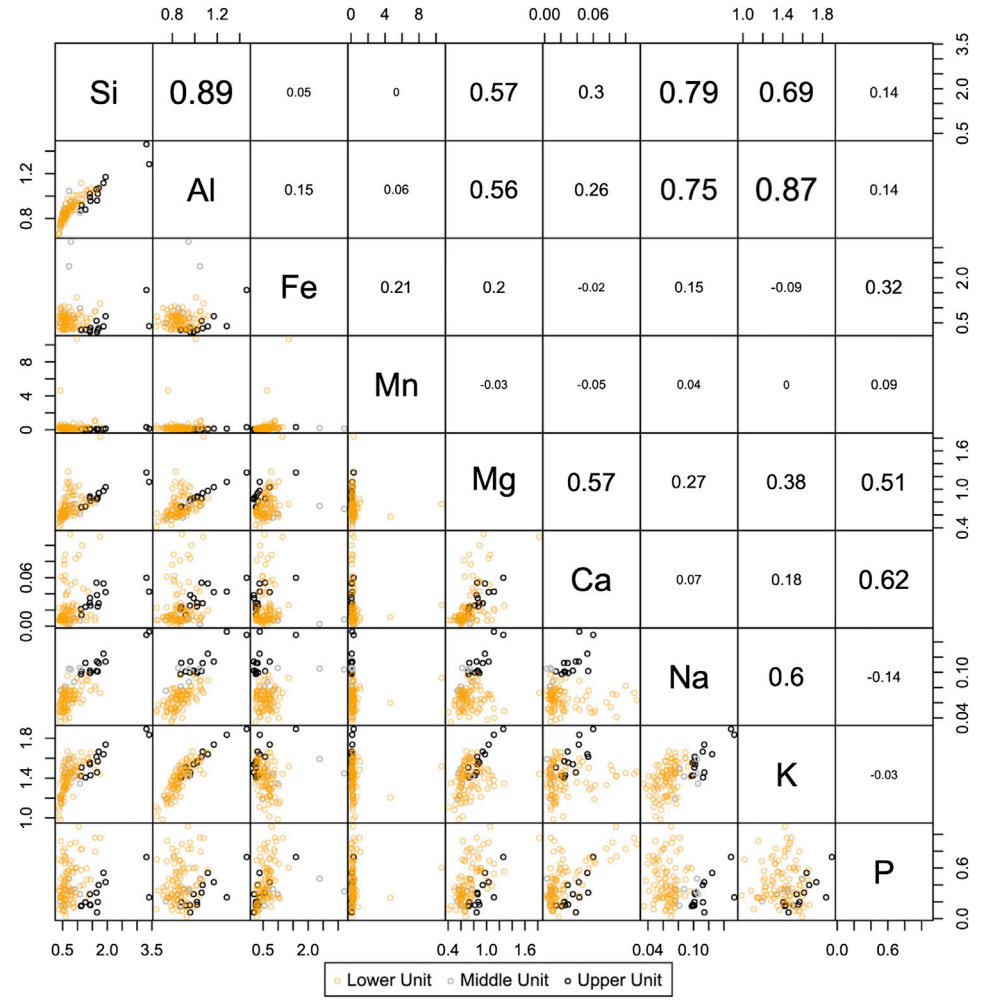

FIGURE 9 | Correlation panel matrix for enrichment factors of major elements. The lower panels in the matrix are scatter plots. The upper panels in the matrix show the correlation coefficients, with font size scaled to the absolute value of each correlation coefficient.

$$\mathrm{MREE/MREE^{*}} = \frac{2 \times (\mathrm{avg.\ MREE/avg.MREE_{PAAS}})}{(\mathrm{avg.LREE/avg.LREE_{PAAS}}) + (\mathrm{avg.HREE/avg.HREE_{PAAS}})},$$

where LREE and HREE represent light REEs (La, Ce, Pr, and Nd) and heavy REEs (Er, Tm, Yb, and Lu), respectively.

The MREE/MREE* ratios throughout the studied section show a pronounced decline in MREE enrichment across the GLT (**Figure 8**). The MREE/MREE* ratios fluctuate between 0.9 and 1.5 during the Wuchiapingian and early Changshingian, but decreased in the late Changshingian.

Cerium has multiple valence states, which results in fractionation that can be quantified by the Ce anomaly (German and Elderfield, 1990; Holser, 1997):

$$\mathrm{Ce/Ce^{*}} = 2\mathrm{Ce_N}/(\mathrm{La_N} + \mathrm{Pr_N}),$$

where the subscript "N" denotes PAAS-normalized values (e.g., $\mathrm{La_N} = \mathrm{La_{sample}/La_{PAAS}}$). If the Ce/Ce* value is lower than 1, Ce is plotted below the line connecting La and Pr, which is called as negative Ce anomaly (**Figure 10**). The Ce/Ce* ratio varies between 0.50 and 1.06, and fluctuates inversely with the MREE/MREE* ratios throughout the studied section (**Figure 8**). With the exception of a few of samples, there is no Ce anomaly (Ce/Ce* ~1) when the REE patterns are relatively flat, but the Ce/Ce* values exhibit negative anomalies in the MREE-enriched samples (**Figure 10**).

Principle Component Analysis

Table 1 provides the component loadings and **Figure 11** shows compositional biplots for the studied samples. We accepted PC1, PC2, and PC3 in this dataset from their eigenvalues (PC1 eigenvalue = 1.960, PC2 eigenvalue = 1.446, and PC3 eigenvalue = 1.179), which explain 81.3% of the total variance (PC1 proportion = 42.7%, PC2 proportion = 23.2%, and PC3 proportion = 15.4%). Other PCs (PC4 and PC5) did not show distinct geochemical components because of their low eigenvalues (<0.8). The loadings of PC1 show strong negative

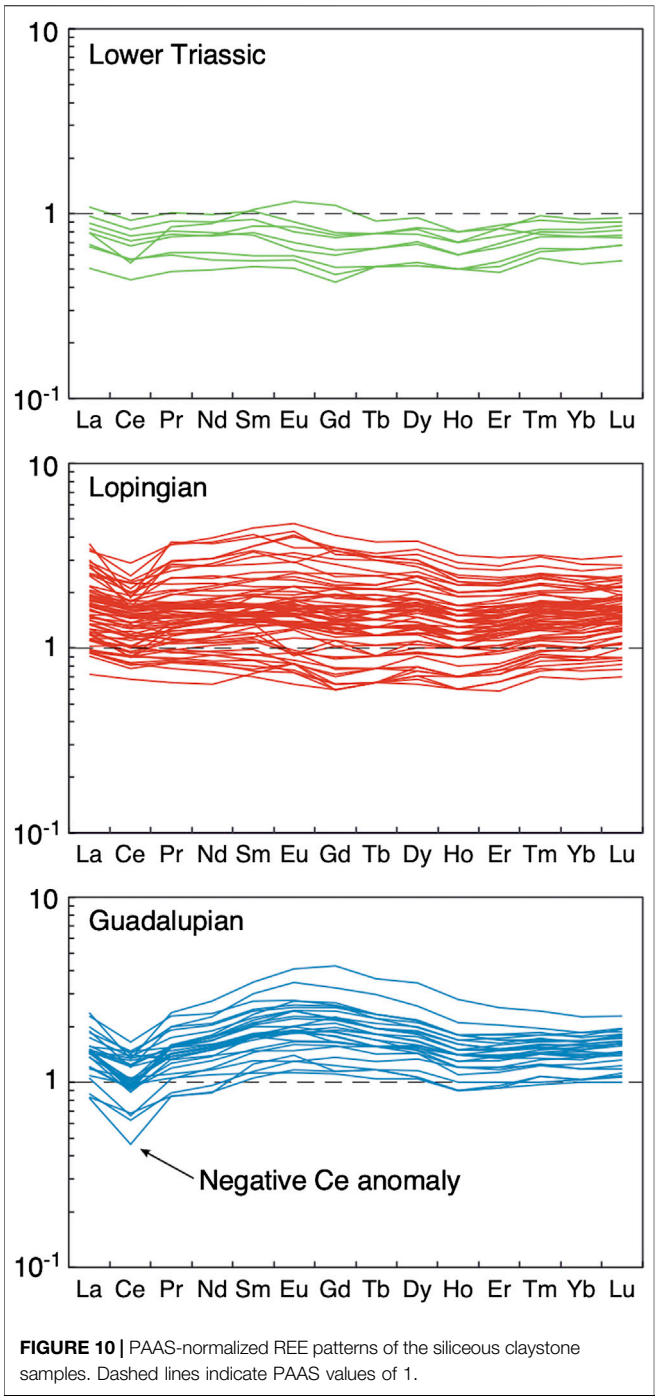

FIGURE 10 | PAAS-normalized REE patterns of the siliceous claystone samples. Dashed lines indicate PAAS values of 1.

values (less than −0.900) for Si and Al, with subordinate negative values (less than −0.700) for Mg, Na, and K, and a moderate negative value for Ca (−0.493). PC2 shows peaks with high negative loadings (less than −0.500) for Fe, Mn and P. PC3 is characterized by a high negative loading for Ca, moderate negative loadings for Mg and P, and positive loadings for all other elements.

The stratigraphic trend of PC1 is relatively constant throughout the Capitanian and largely varies between 0 and 4 in the Wuchiapingian and most of the Changhsingian. However,

TABLE 1 | Principal component loadings calculated from the major element contents of the siliceous claystones.

	PC1	PC2	PC3	PC4	PC5
Si	−0.944	0.051	0.102	0.005	−0.080
Al	−0.948	0.046	0.231	−0.094	0.081
Fe	0.012	−0.813	0.390	0.318	0.099
Mn	0.129	−0.550	0.640	−0.453	−0.238
Mg	−0.739	−0.409	−0.282	0.018	0.159
Ca	−0.493	−0.294	−0.687	−0.126	−0.373
Na	−0.721	0.259	0.374	0.394	−0.296
K	−0.829	0.309	0.118	−0.259	0.271
P	−0.201	−0.840	−0.242	0.047	0.121
Eigenvalue	1.960	1.446	1.179	0.746	0.647
Proportion	42.69	23.22	15.43	6.179	4.657
Cumulative proportion	42.69	65.92	81.35	87.53	92.187

the PC1 scores show an abrupt decrease to negative scores across the EPME and PTB (**Figure 6**). The PC2 scores are characterized by a gradual increase from negative to positive values across the GLT (**Figure 7**). The PC3 scores show a stratigraphic trend in which the Capitanian samples have negative scores, whereas the other Lopingian samples have near-zero or positive scores (**Figure 8**).

INTERPRETATION OF GEOCHEMICAL DATA

Redox-Sensitive Elements

Our geochemical analysis of the upper Guadalupian to Lopingian bedded chert succession from the Iwaidani section records an enrichment in redox-sensitive elements, such as V, Ni, Cu, Zn, Tl, U, Mo. These redox-sensitive elements are divided into two categories on the basis of their behaviors under degrees of marine oxygenation (Calvert and Pedersen, 1993, Calvert and Pedersen, 2007). The first category includes those elements whose valence state varies with the redox environment. Vanadium, U, and Mo form highly soluble ions under oxygenated conditions, but under anoxic and euxinic conditions produce insoluble and particle-reactive materials in their lower valence state (Calvert and Pedersen, 1993; Helz et al., 1996; Zheng et al., 2000; Algeo and Maynard, 2004; Tribovillard et al., 2006; Algeo and Li, 2020). The second category includes elements that are primarily associated with sulfides or Mn-oxide phases. Elements such as Ni, Cu, Zn, and Tl are incorporated into precipitating sulfide phases or scavenged by Fe- and Mn-(oxyhydr)oxides (Calvert and Pedersen, 1993; Rehkämper and Nielsen, 2004; Tribovillard et al., 2006; Calvert and Pedersen, 2007). We use the changes in the enrichment factors, ratios, and contents of these elements as proxies for redox conditions through the studied section.

In the presence of dissolved oxygen, Mn forms insoluble Mn(III) or Mn(IV) hydroxides or oxides (e.g., MnO_2); these particulate forms are rapidly deposited (Calvert and Pedersen, 1993; Sholkovitz et al., 1994). Under suboxic conditions, Mn is reduced to Mn(II) and forms soluble cations (e.g., Mn^{2+} and $MnCl^{+}$) (Algeo and Li, 2020). Since particulate Mn is deposited more readily under oxic conditions, while soluble Mn remains in the water column under suboxic conditions, a low Mn_{EF} (<1) in

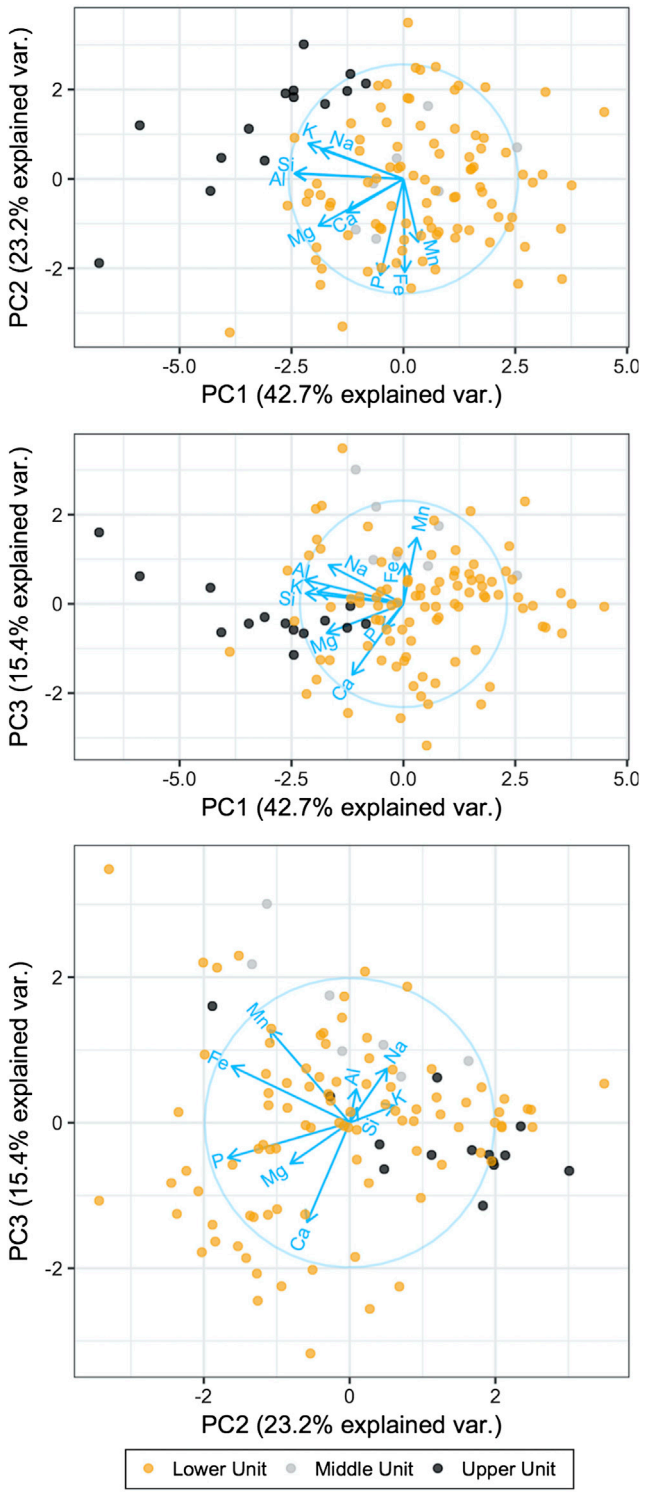

FIGURE 11 | Compositional biplots projected from major elements of the siliceous claystones. Relative directions and lengths of the blue arrows indicate loadings for PC axes. Each variance (var.) is represented as a proportion in this dataset.

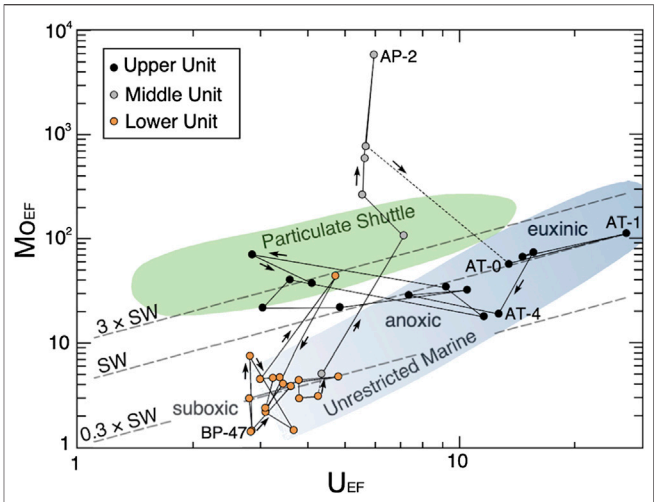

FIGURE 12 | U_{EF} vs. Mo_{EF} diagram for the siliceous claystone samples from lower, middle and upper units of the studied section. Base figure modified from Algeo and Tribovillard (2009).

marine sediments suggest suboxic depositional conditions near the sediment surface. In the Iwaidani section, Mn_{EF} values are generally less than 1, where 1 represents the sample having the exact same ratio as PAAS (**Figure 7**). These Mn_{EF} values are lower than those of the Cisuralian red chert (Sugitani et al., 1991; 0.01–0.10% MnO, 5.2–29 Mn_{EF}), which lies stratigraphically below the studied section (**Figure 2B**; Sano, 1988a). The low Mn values in the Iwaidani section suggest that suboxic conditions has developed in the depositional environment already in the late Guadalupian, long before the PTB.

Vanadium and U enrichments in sediments are proxies for moderately to strongly reducing conditions in the depositional environment (Sadiq, 1988; Algeo and Maynard, 2004; Tribovillard et al., 2006). Vanadium and U reduction occurs under lower oxygen concentrations than Mn reduction (Algeo and Li, 2020). In oxic seawater, V is present as soluble V(V) in the quasi-conservative form of vanadate oxyanions (HVO_4^{2-} and $H_2VO_4^{2-}$). When conditions change from suboxic to weakly anoxic, V(V) converts to V(IV) and forms the vanadyl ion (VO^{2+}), related hydroxyl species [$VO(OH)^{3-}$], and insoluble hydroxides [$VO(OH)_2$] (Breit and Wanty, 1991; Wanty and Goldhaber, 1992). Under H_2S-rich (euxinic) conditions, V(III) is further reduced and precipitates as relatively insoluble hydroxides [$V(OH)_3$] (Wanty and Goldhaber, 1992). Similar to vanadium, soluble U(VI) is reduced to insoluble U(IV) (e.g., UO_2) under anoxic conditions.

In the studied section, Capitanian U_{EF} and V_{EF} values are relatively constant and close to the value of 1 (**Figure 7**). Across the GLT, the V_{EF} and U_{EF} values increase slightly, and then U_{EF} continues to increase during the Changhsingian. The V_{EF} and U_{EF} values increase abruptly in the latest Changhsingian, with peak values at the EPME horizon (**Figure 7**). Similar enrichment trends to those observed here in V and U were observed in Th/U

ratios, another common redox proxy, from end-Permain strata in Italy and Slovenia (**Figure 7**; Wignall and Twitchett, 1996). Consequently, V and U enrichments suggest that the development of suboxic to weakly anoxic conditions occurred across the GLT in this section, followed by anoxic–euxinic conditions during the Changhsingian.

Molybdenum is present in seawater as molybdate (MoO_4^{2-}). Mo-removal from the water column requires the formation of particle-reactive thiomolybdate species ($MoO_xS_{4-x}^{2-}$), which occurs in the presence of aqueous H_2S (Helz et al., 1996; Erickson and Helz, 2000; Helz et al., 2011). Thus, Mo enrichment in sediments requires high H_2S levels in a euxinic environment (Algeo and Tribovillard, 2009; Tribovillard et al., 2012; Algeo and Li, 2020). In the studied section, Capitanian and Wuchiapingian samples have Mo contents below the detection limit (2 ppm). However, our data demonstrate that the Mo_{EF} begins to increase during the lower Changhsingian, which overlaps with the increases in U_{EF} (**Figure 7**). Subsequently, the Mo_{EF} values increase sharply during the latest Changhsingian, with a maximum value of ~5,500. Covariations of the enrichment patterns of Mo and U (Algeo and Tribovillard, 2009; Tribovillard et al., 2012) (**Figure 12**) followed an evolution typical for open marine, hydrographically unrestricted settings (Algeo and Tribovillard, 2009; Tribovillard et al., 2012). Trends in U_{EF} and Mo_{EF} suggest a change from suboxic–anoxic to euxinic conditions in the deep-sea basin during the latest Changhsingian to Induan (**Figure 12**). The Mo_{EF} values in the thousands and Mo_{EF}/U_{EF} ratios in the hundreds are recorded immediately before the EPME (**Figure 7**), suggesting the development of sulphidic bottom water and scavenging of Mo by a Fe–Mn (oxyhydr)oxides particulate shuttle (Algeo and Tribovillard, 2009; Tribovillard et al., 2012). The occurrence of the particulate shuttle requires an oxic–anoxic redox boundary in the water column and rapid water replacement to maintain the predicted Fe–Mn redox behavior (Algeo and Tribovillard, 2009; Scholz et al., 2013). However, redox boundaries and vertical circulation in the pelagic Panthalassa remain unclear, and this needs to be addressed in future studies.

Ni, Cu, Zn, and Tl are incorporated into precipitating sulfide phases or scavenged by Fe- and Mn-(oxyhydr) oxides (Calvert and Pedersen, 1993; Koschinsky and Hein, 2003; Algeo and Maynard, 2004; Rehkämper and Nielsen, 2004; Tribovillard et al., 2006; Calvert and Pedersen, 2007). Since the entire section contains low Mn-enrichment factors (Mn_{EF} <1), except for two high-Mn_{EF} peaks (Mn_{EF} >6) in the Changhsingian (~13.5–14.5 m), enrichment patterns for Ni, Cu, Zn, and Tl may be related to authigenic sulfides (e.g., pyrite) in a reducing environment (Huerta-Diaz and Morse, 1992; Morse and Luther, 1999; Tribovillard et al., 2006; Belzile and Chen, 2017). In the studied section, Ni_{EF}, Cu_{EF}, Zn_{EF}, and Tl_{EF} begin to increase in the lower Changhsingian and remain high until the uppermost Changhsingian (**Figure 7**). This supports increasingly anoxic and/or euxinic bottom water conditions toward the latest Changhsingian, as suggested by the V_{EF}, U_{EF}, and Mo_{EF} values. Relatively high Tl_{EF} values are recorded in the stratigraphic interval from ~13.5 to 14.5 m, which appears to be associated with Mn enrichment (Koschinsky and Hein, 2003).

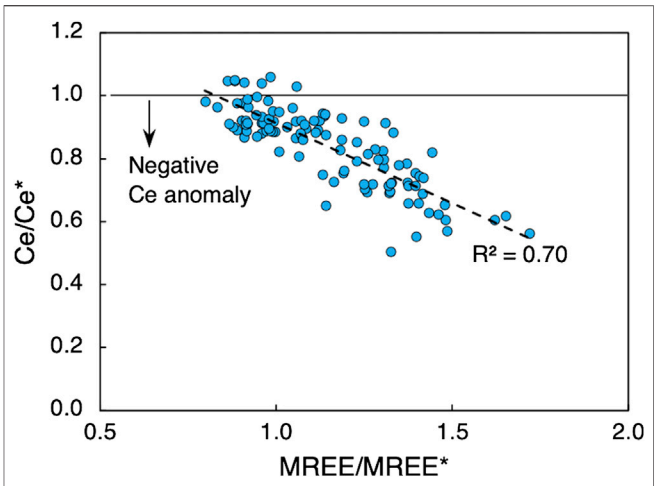

FIGURE 13 | Crossplot of Ce/Ce* vs. MREE/MREE* for the siliceous claystone samples.

In addition to the redox-sensitive elements mentioned above, the Ce anomaly is also a common tracer for redox conditions in pelagic sediments (Kato et al., 2002; Takahashi et al., 2014; Fujisaki et al., 2019). Our data reveal that low Ce/Ce* values are associated with increased MREE (**Figure 13**), and there is no Ce anomaly when the REE patterns are relatively flat in the studied section (**Figures 8**, **10**). Since the MREE-enriched patterns are probably due to the presence of fossilized biogenic apatite (e.g., conodonts) that recrystallized during diagenesis (Reynard et al., 1999; Chen et al., 2015; Zhang et al., 2016), the stratigraphic trends of Ce/Ce* values in the Iwaidani section may reflect the change in biogenic apatite content during diagenesis, rather than recording the redox conditions.

Principal Components

The PC1 scores of the present study represent the compositional variations in terrigenous detrital materials (aluminosilicates), because the loadings show strong negative values for Si, Al, Mg, Ca, Na, and K (**Table 1**). Prominent negative loadings for both Si and Al and the strong positive correlation coefficient between Si_{EF} and Al_{EF} (r = 0.89; **Figure 9**) indicate PC1 is related to the presence aluminosilicates, such as clay minerals. The same directions in the relatively strong loadings for alkali and alkaline Earth elements (Mg, Ca, Na, and K) with those of Si and Al suggest that these elements have been substituted for Si–Al units and layers or Al octahedral sheets in clay minerals (e.g., Brigatti et al., 2006). Thus, these elemental behaviors in the PC1 axis indicate the intensity of chemical weathering.

To verify the PC1 interpretation, we employed the chemical index of alteration (CIA; Nesbitt and Young, 1982) and the weathering index of Parker (WIP; Parker, 1970). These indices are widely used for reconstructing paleoclimate conditions by assessing the degree of hinterland weathering, which is controlled mainly by climatic factors (Nesbitt and Young, 1982; Nesbitt et al., 1996; Ohta and Arai, 2007; Sheldon and Tabor, 2009; Yang

et al., 2016). Values of CIA indicate the extent of decomposition of feldspar minerals, which are the most abundant mineral group in the upper continental crust (Taylor and McLennan, 1985). The CIA is defined as $Al_2O_3/(Al_2O_3 + CaO^* + Na_2O + K_2O) \times 100$ (molar content). CaO in silicate phases (CaO^*) is estimated by subtracting CaO in phosphate phases, predicted from P_2O_5 contents (McLennan, 1993; Price and Velbel, 2003). In samples with low CaO and high P_2O_5 contents, this calculation may yield negative values. In this case, values are set to 0. The WIP is defined as $100 \times (2Na_2O/0.35 + MgO/0.9 + 2K_2O/0.25 + CaO^*/0.7)$ (molar content). We used WIP to assess the weathering intensity of silicate rocks based on the proportions of alkali and alkaline Earth elements in the weathered products (Parker, 1970). The smaller WIP values denote stronger chemical weathering, which is opposite to the CIA values.

Figure 6 shows stratigraphic variations in CIA, WIP, and PC1. The stratigraphic profile of the PC1 scores correlates well with the WIP profile, supporting the interpretation that PC1 reflects the intensity of hinterland weathering. The general trend of the CIA index is also similar to that of PC1. The PC1 scores decrease with increasing CIA and decreasing WIP values across the EPME, suggesting intensified chemical weathering in hinterland areas during the latest Changhsingian to earliest Induan.

The PC2 scores explain the accumulation of Fe (oxyhydr) oxides in the section, because of the strong negative loadings (< −0.800) of Fe and P (**Table 1**). Negative P loading suggests adsorption or co-precipitation of phosphate on sinking Fe-oxyhydroxide particles (e.g., FeOOH–PO_4 particles; Yao and Millero, 1996; Dellwig et al., 2010). In addition, relatively strong loading of Mn may also result from adsorption and/or co-precipitation of Mn as a particulate in the Mn–Fe–P-shuttle (MnOx–FeOOH–PO_4; Dellwig et al., 2010). Such Fe- and P-rich particles are reductively dissolved under anoxic–euxinic conditions, and release Fe^{2+} and phosphate to the water column (Shaffer, 1986; Dellwig et al., 2010). The correlation coefficient between Fe_{EF} and P_{EF} under the anoxic–euxinic conditions during the Changhsingian and Induan (r = 0.30) is lower than that of the Capitanian and Wuchiapingian (r = 0.62). The more negative PC2 scores (**Figure 7**) suggest a greater accumulation of Fe- and P-rich particles in a more oxygen-rich environment under the suboxic conditions of the Capitanian and early Wuchiapingian, but this interpretation is not valid under the anoxic–euxinic conditions after the late Wuchiapingian.

The PC3 axis explains the calcium phosphate accumulation, because the loadings show relatively strong negative values for both P and Ca in the compositional biplot (**Figure 11**). The enrichment factors for Ca and P show a relatively strong positive correlation (r = 0.62; **Figure 9**) that is consistent with the occurrences of conodont fossils in the studied section (Sano et al., 2012a). Indeed, the stratigraphic trends in P_{EF} and Ca_{EF} are largely similar to those in PC3 (**Figure 8**). Thus, these characteristics of PC3 are related to biogenic apatite accumulation, as reported from multivariate statistical analyses of a Middle Triassic bedded chert succession in the Mino Belt, Japan (Soda and Onoue, 2019). The more negative direction of the PC3 scores indicate the presence of biogenic apatite, because the loadings of P and Ca have the same directions (negative). Therefore, negative PC3 scores in the Capitanian (**Figure 8**) imply higher accumulations of biogenic apatite, whereas the near-zero PC3 scores in the Wuchiapingian to Induan samples suggest minor contributions of biogenic apatite to the sediments. Ca_{EF} and P_{EF} are relatively high in the Capitanian and clearly decrease across the GLT, which supports this interpretation of PC3. Indeed, the REE patterns in the Capitanian samples display a moderate to high enrichment in MREE (**Figure 8**), which is probably due to the presence of fossil biogenic apatite that recrystallized during diagenesis (Reynard et al., 1999; Chen et al., 2015). Thus, the relative depletion of MREEs in the Wuchiapingian samples is probably due to the paucity of biogenic apatite, which is consistent with the interpretation that the decrease in PC3 was associated with decreased contents of biogenic apatite across the GLT.

DISCUSSION

Based on the geochemical interpretations of redox-sensitive elements and principal components from the Iwaidani section, we discuss the redox history of the Guadalupian–Lopingian deep-sea Panthalassa, and compare our results with the PTB section at Gujo-Hachiman, where deep-sea oxic-dominated conditions have been proposed for the same period (Wignall et al., 2010; Fujisaki et al., 2019). We also investigate the environmental changes that affected the oceanic redox conditions using the results from our PCA.

Redox History

The detailed redox history of the Iwaidani section, from the Capitanian to Induan, is summarized in **Figure 14**. The entire section shows a low enrichment factor for Mn (Mn_{EF} <1), suggesting that reducing conditions has developed in the depositional environment already in the Capitanian. The enrichment patterns of the other redox-sensitive elements show a stepwise development of oxygen-depleted conditions in the studied section, referred to here as stages 1, 2, and 3 (in ascending order) (**Figure 14**).

Stage 1 consists of a slight enrichment of V and U (~1.5–2.0 times that of the Capitanian), suggesting the initiation and development of reducing conditions across the GLT (**Figure 14**). The stratigraphic variations in PC2 scores indicate that the accumulation of Fe- and P-rich particles decreased across the GLT, suggesting the depositional environment changed from suboxic to weakly anoxic conditions, meaning that these particles could have been reductively dissolved. Subsequently, increases in U_{EF}, Mo_{EF}, Ni_{EF}, Cu_{EF}, Zn_{EF}, and Tl_{EF} during stage 2 indicate the development of anoxic conditions, which began at the WCB transition. Stage 3 (latest Changhsingian) is characterized by marked enrichments in Mo contents. The Mo_{EF} values and Mo_{EF}/U_{EF} ratios (**Figure 7**) demonstrate that H_2S-rich (euxinic) conditions may have developed in the latest Changhsingian, concurrent with the EPME. Since the average sedimentation rate for the Changhsingian bedded chert of the

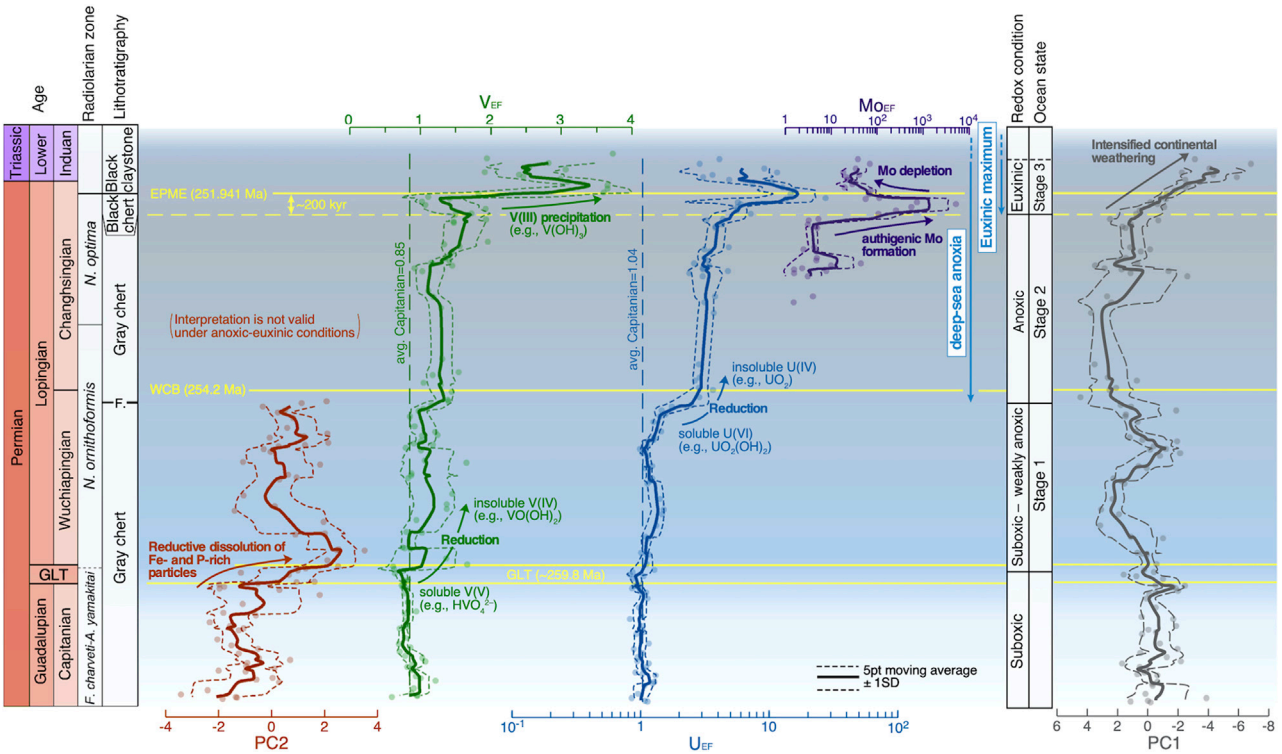

FIGURE 14 | Redox history of the Guadalupian to Lower Triassic deep-sea Panthalassa inferred from redox-sensitive elements (V, U, and Mo) and PC scores (PC1 and PC2) in the studied section. The Lopingian shows a stepwise development (stages 1 to 3) of prolonged oxygen-depleted conditions (i.e., deep-sea anoxia; Isozaki, 1997). Euxinic conditions in stage 3 began ~200 kyr before the EPME, corresponding to the "euxinic maximum" reported from the Akkamori section in Japan (Takahashi et al., 2014). PC1 data show that euxinic conditions developed at the same time as an intensification of continental weathering, both of which began ~200 kyr before the EPME.

Hashikadani Formation is ~0.3 cm·kyr^{-1} (Onoue et al., 2019), the anomalous increases in Mo_{EF} corresponding to the 60 cm stratigraphic interval at the end of the Permian indicate that the euxinic conditions in stage 3 began ~200 kyr before the EPME (**Figure 14**). The increase in V_{EF} and U_{EF} does not coincide with the increase in Mo_{EF}, and their values increase significantly at the EPME horizon (**Figure 7**). Since Mo is adsorbed onto Fe–Mn particulates, whereas U and V are not, this pattern is consistent with the development of a particulate shuttle (Algeo and Tribovillard, 2009) immediately before the EPME. The appearance of a particulate shuttle at that time has also been reported from the Akkamori section in Northeast Japan (Takahashi et al., 2014). The development of the particulate shuttle in the pelagic Panthalassa may have depended on development of redox boundaries and vertical circulation in the early phase of stage 3, and this needs to be addressed in future studies.

Our redox-sensitive element data and PCA are consistent with previous interpretations of the gradual expansion of reducing conditions starting around the GLT (Isozaki, 1997; Kato et al., 2002). Isozaki, 1994 and Isozaki, 1997 coined the term "deep-sea anoxia" to describe this unique long-term oceanographic phenomenon in the deep sea of the mid-Panthalassa. In this study, we have newly identified three distinct ocean states (stages 1–3) during the Lopingian. Our results support the hypothesis of deep-sea anoxia, but contradict recent interpretations of oxic-dominant conditions in deep-sea Panthalassa during the Lopingian, as evidenced by positive Ce anomalies and limited increases in U and Mo from the PTB section at Gujo-Hachiman (Algeo et al., 2010; Algeo et al., 2011b; Fujisaki et al., 2019). The differences in redox conditions between the Iwaidani and Gujo-Hachiman sections are discussed below, in Section *Anoxic vs. Oxic Condition in Deep-Sea Panthalassa*.

Furthermore, the present study demonstrates that the changes from suboxic to euxinic conditions through the Lopingian reach a maximum immediately before the EPME. Takahashi et al. (2014) provided evidence of such euxinic conditions in the deep sea of the central Panthalassa Ocean immediately before and during the EPME, as evidenced by extremely high concentrations of U and Mo (enrichment factors of ~6 and ~7,600, respectively) in the uppermost Changhsingian black claystone from the Akkamori section in Northeast Japan (**Figure 1B**). Their values are consistent with those from the black claystone bed (~6 U_{EF}, ~5,500 Mo_{EF}) at the top of the middle unit in the Iwaidani section. These studies suggest that the "euxinic maximum" (Takahashi et al., 2014) at the end of the Permian is most likely a phenomenon that occurred on the deep seafloor of the Panthalassa Ocean (**Figure 14**). Subsequent abrupt decreases in U_{EF} and Mo_{EF} are recorded by the Induan black claystones in the Iwaidani section. Similar decreases in U_{EF} and Mo_{EF} after the

EPME have also been reported for the pelagic deep-sea PTB section at Akkamori. The concurrent drawdown of U_{EF} and Mo_{EF} in both sections might reflect a drawdown of these trace elements in the global oceanic inventory (Takahashi et al., 2014).

Anoxic vs. Oxic Condition in Deep-Sea Panthalassa

Oxygen-depleted conditions during the latest Changhsingian have been proposed from other pelagic deep-sea PTB sections in Japan, such as the Waidani, Gujo-Hachiman, Akkamori, Ubara, and Tenjinmaru sections (**Figure 1B**; Kajiwara et al., 1994; Algeo et al., 2010; Wignall et al., 2010; Algeo et al., 2011b; Sano et al., 2012b; Takahashi et al., 2014; Kaiho et al., 2016; Zhang et al., 2017; Onoue et al., 2019). Of these, the Waidani, Akkamori, Ubara, and Tenjinmaru sections have limited stratigraphic records from the late Changhsingian to Early Triassic, whereas the Gujo-Hachiman section preserves a longer record from the Capitanian to the latest Changhsingian (Algeo et al., 2010; Zhang et al., 2017; Fujisaki et al., 2019). Therefore, here we discuss the redox conditions in the Lopingian by comparing the Iwaidani and Gujo-Hachiman sections.

The Gujo-Hachiman section (Kuwahara, 1997; Kuwahara et al., 1998) in the Mino Belt crops out ~18 km east of the Iwaidani section (**Figure 2B**). Several large slabs (~2–5 km wide and ≥15 km long) of ocean-island basalts and carbonate rocks are distributed between the Iwaidani and Gujo-Hachiman sections, and the rocks of both sections originated on a mid-oceanic seamount in the Panthalassa Ocean (Sano, 1988a, Sano, 1988b; Sano, 1989; Jones et al., 1993; Ichiyama et al., 2008). Therefore, both PTB sections are interpreted as pelagic facies that extend from the deep-ocean floor to the lower flank of a mid-Panthalassic seamount. This is evidenced by thin intercalations of dolomite rocks in the lower Guadalupian bedded cherts at Gujo-Hachiman (Kuwahara et al., 1998), which are likely reworked deposits from a shallow-water carbonate buildup, as previously suggested by Sano (1988a). Biostratigraphic analysis of radiolarians and conodonts revealed that the Gujo-Hachiman section contains the GLT and WCB (Kuwahara et al., 1998; Yao et al., 2001; Nishikane et al., 2011; Nishikane et al., 2014).

Recent studies of redox-sensitive elements (e.g., U, Mo, and Ce) and the quantitative analysis of framboidal pyrite from the Gujo-Hachiman section suggest oxic-dominant conditions in the deep-sea during the Lopingian and a rapid expansion of the sulphidic OMZ at shallower depths immediately before the EPME (Algeo et al., 2010; Wignall et al., 2010; Fujisaki et al., 2019). Based on positive Ce anomalies and low Mo and U enrichment factors, Fujisaki et al. (2019) suggested that the Gujo-Hachiman section records well-oxygenated conditions of deep-sea Panthalassa during the Guadalupian and most of the Lopingian, and episodic occurrences of suboxic conditions during the middle–late Lopingian.

These studies contradict our interpretation of the stepwise development of suboxic–euxinic conditions during the Lopingian (**Figure 14**), even though the Iwaidani and Gujo-Hachiman sections are located near each other and thus their depositional environments should have been similar. Since Mo-U co-variance trends for the Iwaidani section reflect open-marine, hydrographically-unrestricted depositional settings (**Figure 12**), it is unlikely that only the sediments in the Iwaidani section were deposited under restricted basin with stagnant conditions around a mid-oceanic seamount.

We suggest that the cherts and siliceous claystones from the Gujo-Hachiman section are intensely altered by the intrusions of nearby Cretaceous rhyolites and felsites (**Figure 2B**) and may not record the redox conditions in the Guadalupian and Lopingian. In previous studies, red hematite nodules have been described throughout the Gujo-Hachiman section, which has been referred to as negative evidence for anoxic conditions (Wignall et al., 2010). However, outcrop observations indicate that the hematite nodules with irregular shape and margins occur in association with the development of white and red veins and vugs of possible hydrothermal origin (**Supplementary Figure S1**). The development of these nodules and veins is characteristic of the Permian chert beds at Gujo-Hachiman and is not found in other Permian sections of the Funabuseyama area (Sano, 1988a; Sano, 2018). It is possible that the nodules and veins characteristic of the Gujo-Hachiman section were formed by the intrusions of the Cretaceous Okumino rhyolites distributed around the section (**Figure 2B**). Although their origin needs further investigation, the development of such veins is likely to significantly alter the chemical compositions of the siliceous claystone samples from the Gujo-Hachiman section.

In general, the correlations of Al, K and Rb contents attributed to alluminosilicates (mainly clay minerals) are strong in the bedded charts of the Mino Belt (Kato et al., 2002; Soda and Onoue, 2018, Soda and Onoue, 2019; Sato et al., 2020), and high correlations of these elements are also found in the Iwaidani section (**Figures 5**, **9**). This implies that Al, K, and Rb in alluminosilicate minerals in the Permian bedded cherts were not significantly mobilized during post-depositional alteration processes. In contrast, there is no clear correlation between Al, K, and Rb in the Gujo-Hachiman section (**Supplementary Figure S2**). Compared with Iwaidani, the Gujo-Hachiman section shows a depletion of K and Rb relative to Al, but instead contains an excess of Si and Fe. This may indicate that the leaching of alkaline elements (K and Rb) and precipitation of Si and Fe occurred due to hydrothermal alteration (Pirajno, 2009). Chemical weathering indices (CIA and WIP) are sensitive to changes in bulk chemistry that is also associated with hydrothermal alteration (Price and Velbel, 2003; Pirajno, 2009). In contrast to the Iwaidani section, the Gujo-Hachiman samples are characterized by highly variable CIA and WIP values (**Supplementary Figure S3**) with highly to completely weathered nature (e.g., CIA >80, WIP <20; Duzgoren-Aydin et al., 2002; Ohta and Arai, 2007), suggesting that the samples are subjected to strong chemical alteration, probably due to hydrothermal alteration and accentuated weathering. If this interpretation is correct, elemental redox proxies, such as V and U, may have been affected by the chemical alterations, including oxidation leaching of these elements during hydrothermal alteration. Further geochemical and mineralogical studies are needed to constrain these interpretations.

The much higher U_{EF} and Mo_{EF} values, indicative of euxinia, are also observed in the latest Changhsingian at the Iwaidani

section but not in the Gujo-Hachiman section. Algeo et al. (2011b) suggested that the bottom water of the Gujo-Hachiman section was suboxic, as evidenced by the limited increases in V, U, and Mo across the chert–black shale facies transition. This may reflect the hydrothermal alterations (as discussed above), but the lack of a stratigraphic record corresponding to the euxinic condition may be a more realistic explanation of this difference (Takahashi et al., 2014). As shown in **Supplementary Figure S4**, the rocks in the uppermost Changhsingian are strongly deformed compared with the lower stratigraphic intervals of the section. The Gujo-Hachiman section lacks the Hg/TOC anomalies and negative $\Delta^{33}S$ anomalies found at the uppermost Changhsingian in other PTB sections in Japan (Zhang et al., 2017; Shen et al., 2019), which can be explained by the absence of the stratigraphic interval corresponding to the euxinic conditions, due to minor shear faults at Gujo-Hachiman (**Supplementary Figure S4**). This explanation was also proposed by Takahashi et al. (2014) and Kaiho et al. (2016) to explain the different redox conditions between the Gujo-Hachiman and Akkamori sections during the latest Changhsingian.

Based on quantitative analyses of the framboidal pyrite size distribution, Algeo et al. (2010) and Wignall et al. (2010) suggested that a shallow-water sulphidic OMZ rapidly expanded immediately before the EPME. If this were the case, evidence of a shallow water OMZ should be found in the Iwaidani section. However, our interpretation of redox conditions based on our trace element data does not provide evidence on the position of chemoclines in the water column. Future geochemical research, such as iron speciation, total sulfur and stable sulfur isotopic composition, and the size of pyrite grains, will help confirm or refute this hypothesis (Wignall et al., 2010; Zhang et al., 2017; Takahashi et al., 2019; Maruoka and Isozaki, 2020).

Enhanced Hydrological Cycle and Ocean Anoxia

Previous studies have suggested that the release of volcanic and contact metamorphism-related gases (CO_2 and CH_4) from the Siberian Traps would have enhanced global warming just before the PTB, which is supported by oxygen-isotope studies of marine biogenic calcite and apatite (Kearsey et al., 2009; Sun et al., 2012; Chen et al., 2016). The resulting temperature increase and the collapse of vegetation on land may have resulted in intensified chemical weathering via acceleration of the hydrological cycle (Sephton et al., 2005; Algeo and Twitchett, 2010; Sun et al., 2018), which would have caused increased nutrient discharge (e.g., nitrates and phosphates) to the global ocean and a resulting increase in primary productivity, leading to global oceanic anoxic conditions (Wignall, 2007; Algeo et al., 2011a; Zhang et al., 2018b; Schobben et al., 2020).

During stage 3, the siliceous rocks of the Iwaidani section record evidence for enhanced chemical weathering accompanied by a change from anoxic to euxinic conditions (**Figure 14**). Our study shows negative PC1 scores with increasing CIA and decreasing WIP values across the PTB, implying intensified chemical weathering in hinterland regions during the latest Changhsingian to earliest Induan. Given that the average sedimentation rate of the Changhsingian bedded chert is ~0.3 cm·kyr^{-1} (Onoue et al., 2019), enhanced continental chemical weathering occurred ca. 200 kyr before the EPME. These results support the interpretation of an acceleration of the hydrologic cycle and increased weathering rates immediately before the PTB, as evidenced by geochemical, biomarker, and isotopic studies (Sephton et al., 2005; Sheldon, 2006; Algeo and Twitchett, 2010; Kaiho et al., 2016; Sun et al., 2018; Cao et al., 2019).

The shift to a warmer climate during the transition between anoxic and euxinic depositional environments is also supported by the decrease in the enrichment factors of Ti, Zr, and Hf (**Figure 6**), which are primarily concentrated in heavy mineral assemblages such as ilmenite, rutile, titanomagnetite, and zircon (Schmitz, 1987; Shimmield and Mowbray, 1991; Calvert and Pedersen, 2007). Because the distribution of heavy minerals in deep-sea sediments is affected by changes in the grain size of wind-blown dust, the enrichments of these elements indicate increases in the intensity of aeolian transport and wind strength (Boyle, 1983; Beveridge, 1994; Calvert and Pedersen, 2007). Previous studies on past atmospheric transport of terrestrial materials (Rea et al., 1985; Rea, 1994; Anderson et al., 2006) suggest that decreases in Ti_{EF}, Zr_{EF}, and Hf_{EF} may reflect a transition to a more humid climate, and more specifically to humid conditions within the dust source regions and/or precipitation along the pathways of dust transport. Consequently, our results suggest that the climate changed to relatively warm and humid conditions during the ca. 200 kyrs prior to the EPME. The causes of this climatic change are debated, and hypotheses include an extraterrestrial influence on the influx of interplanetary dust particles (Onoue et al., 2019; Takahata et al., 2019); however, large-scale eruption of the Siberian Traps is commonly favored to explain the global warming and rapid enhancement of continental weathering (Wignall, 2007; Algeo et al., 2011a; Schobben et al., 2020). Two-thirds of the total lava volume of the Siberian Traps was deposited ca. 300 kyr before the EPME (Burgess and Bowring, 2015; Burgess et al., 2017). Grasby et al. (2011) suggested that a release of coal fly-ash generated by magma-coal thermal metamorphism in the Siberian Traps, which was dispersed globally during the 500–750 kyr before the EPME. Therefore, it seems reasonable to assume that intensified continental weathering indicated by our PC1 and weathering proxy data was related to initial emplacement of the Siberian Traps before the EPME.

In theory, enhanced chemical weathering via acceleration of the hydrological cycle would cause increased nutrient discharge (e.g., nitrates and phosphates) to the global ocean, with a consequent increase in biological productivity (Jones and Jenkyns, 2001; Jenkyns, 2010; Pogge von Strandmann et al., 2013). Elevated values of total organic carbon (TOC) and paleoproductivity proxy data (e.g., Ba and P) in PTB black claystones in Japan have been cited as evidence of increased primary productivity across the PTB in the Panthalassa Ocean (Suzuki et al., 1998; Algeo et al., 2011b), though nitrogen and carbon isotope data along the northwestern margin of Pangea (Grasby et al., 2016) and the eastern margin of the Panthalassa (Schoepfer et al., 2013)

suggest nutrient-limited conditions and reduced primary productivity in the earliest Triassic. Barium is commonly used as a tracer of paleoproductivity (Zachos et al., 1989; Dymond and Collier, 1996; McManus et al., 1998; Algeo et al., 2011b), since barite precipitation occurs in decaying particulate organic matter while it sinks to the seafloor (Dehairs et al., 1980; Bishop, 1988; Dymond and Collier, 1996), which is supported by enhanced Ba_{EF} values below high-productivity areas (Nürnberg et al., 1997). Our data show that Ba_{EF} decreased significantly during the Wuchiapingian and then remained consistently low until the Induan (**Figure 8**). Thus, the Iwaidani section demonstrates no apparent link between increased chemical weathering and paleoproductivity during the latest Changhsingian. However, Ba cannot be used as a proxy for paleoproductivity under anoxic to euxinic conditions because 1) low sulfate concentrations in seawater, which are inferred for the late Permian–Early Triassic (Bottrell and Newton, 2006; Luo et al., 2010), reduce the solubility product of barite in seawater; and 2) anoxic conditions in sediment pore water cause the reductive dissolution of sedimented barite (Algeo et al., 2011b). Since the stratigraphic profile of Ba_{EF} mimics that of Th/U ratios and is inversely correlated with U_{EF} (**Figures 7**, **8**), Ba_{EF} might not record variations in paleoproductivity, but instead reflect the dissolution of barite in the anoxic–euxinic environments during the Changhsingian and Induan. Consequently, the variation in paleoproductivity in relation to increased chemical weathering could not be investigated in the Iwaidani section, and the causal connection between chemical weathering and the development of euxinic conditions during the latest Changhsingian remains unclear. We need further investigation, such as carbon and nitrogen isotope analyses, to evaluate this connection.

Like the PTB, climate change induced by large-scale volcanism has also been proposed for the Capitanian (e.g., Wignall et al., 2009; Bond et al., 2010). The Emeishan Traps in South China were identified as a possible cause of the global warming during the late Capitanian (Chen et al., 2011); thus, enhanced chemical weathering during this period is expected (Zhang et al., 2019). However, the PC1 scores in the Iwaidani section did not change during the Capitanian and earliest Wuchiapingian (**Figure 14**). Chen et al. (2011), Chen et al. (2013) used oxygen isotopes from conodonts and found an increase in the paleotemperature during the late Capitanian, which reflects the end-Guadalupian global regression (Haq and Schutter, 2008) and shallowing of conodont habitats. This interpretation appears to be more appropriate in explaining the increase in seawater temperature in South China during the late Capitanian.

Our data reveal that suboxic to weakly anoxic conditions developed ca. 8 Myr prior to the PTB. There is no simultaneous increase in chemical weathering recorded by the negative PC1 scores during the prolonged suboxic–anoxic conditions in the Lopingian, except near the PTB (**Figure 14**). The cause of the onset of deep-sea anoxia remains uncertain, but our new data largely exclude the possibility that the event was induced by abrupt warming and subsequent acceleration of the hydrological cycle, triggered by degassing related to large-scale volcanic activity. The weakening of ocean circulation with the end of the Gondwana glaciation and Kamura cooling event (Isozaki et al., 2007a; Isozaki et al., 2007b) might be one possible explanation for a relatively stagnant ocean (Kajiwara et al., 1994; Isozaki, 1997) that led to the development of deep-sea anoxia during the Lopingian. Across the GLT, a decrease in the PC3 scores was associated with decreased concentration of biogenic apatite, which is sourced primarily from conodonts and pelagic vertebrates such as fish. Regions of upwelling around seamounts exhibit increased nutrient concentrations in surface waters, which result in the proliferation of fish in pelagic realms (Ohta et al., 2020). The decreasing PC3 trend in this study may therefore reflect the weakening transport of deep nutrient-rich cold water to the surface around the seamount by oceanic upwelling, due to more stagnant ocean circulation. However, a causal link between a reduced nutrient supply and conodont productivity has not been found. Further geological and geochemical research is needed to verify the exact nature of the deep-sea anoxia.

CONCLUSION

Redox changes in the Guadalupian (middle Permian) to Lower Triassic bedded chert succession from the Iwaidani section, Japan, were inferred on the basis of stratigraphic variations in redox-sensitive elements (e.g., Mn, V, Mo, and U). We also applied PCA to major element compositions to investigate the environmental changes that triggered the oceanic redox changes. The Permian/Triassic boundary section that was examined in this study extends from pelagic deep-sea facies deposited on the ocean floor to the lower flank of a mid-Panthalassan seamount.

Our data reveal that the enrichment patterns of redox-sensitive elements are characterized by a three-stage increase (stages 1 to 3) during the Lopingian. Stage 1 is characterized by slight enrichments of V and U across the transition between the Guadalupian and Lopingian, suggesting the initiation of oxygen-poor conditions ca. 8 Myr prior to the Permian/Triassic boundary. Subsequently, anoxic conditions developed during the late Wuchiapingian (stage 2), as inferred from increases in the enrichments of U, Mo, Ni, Cu, Zn, and Tl. Stage 3 shows strong enrichments in V, U, and Mo, which indicates that euxinic conditions developed in the latest Changhsingian and around the time of the end-Permian mass extinction event. These results demonstrate the development of prolonged oxygen-depleted conditions ("deep-sea anoxia") in the Lopingian deep-sea Panthalassa Ocean.

We extracted three PCs from the major element compositions of 114 siliceous claystone samples from the study section. PC1, PC2, and PC3 indicate the influence of chemical weathering intensity, Fe-rich (oxyhydr)oxides particles, and biogenic apatite, respectively, on the bulk sediment geochemistry. The stratigraphic variations of the PC2 scores indicate that the accumulation of Fe-rich particles decreased across the GLT, suggesting a change in depositional environment from suboxic to weakly anoxic conditions (stage 1), meaning that these particles would have been reductively dissolved. The PC3 score shows a decline in apatite-secreting organisms accompanied by the development of reducing conditions in stage 1. The cause of the onset and development of deep-sea

anoxia during stages 1 and 2 remains unresolved; however, our PC1 and weathering proxy data suggest that the development of euxinic conditions in the latest Changhsingian (stage 3) was triggered by intensified continental weathering in response to a temperature rise ca. 200 kyr before the EPME.

DATA AVAILABILITY STATEMENT

The original contributions presented in the study are included in the article/**Supplementary Material**, further inquiries can be directed to the corresponding author.

AUTHOR CONTRIBUTIONS

TO and YI designed the study. KS performed the PCA. All authors participated in the discussion and interpretation of the analytical results and aided in the writing of the manuscript.

FUNDING

This study was supported by the Japan Society for the Promotion of Science (grants JP20H00203 to TO and JP19H00711 to YI).

ACKNOWLEDGMENTS

We thank H. Sano and K. Kuwahara for information on the Iwaidani and Gujo-Hachiman sections. We also thank M. Murai, the manager of the Iwaidani gully logging road, who offered us facilities for fieldwork.

SUPPLEMENTARY MATERIAL

The Supplementary Material for this article can be found online at: https://www.frontiersin.org/articles/10.3389/feart.2020.613126/full#supplementary-material.

REFERENCES

Aitchison, J., and Shen, S. M. (1980). Logistic-normal distributions—some properties and uses. *Biometrika*. 67, 261–272. doi:10.2307/2335470

Aitchison, J. (1986). *The statistical analysis of compositional data*. London, United Kingdom: Chapman and Hall.

Albarède, F. (1995). *Introduction to geochemical modeling*. Cambridge, United Kingdom: Cambridge University Press.

Algeo, T. J., Chen, Z. Q., Fraiser, M. L., and Twitchett, R. J. (2011a). Terrestrial–marine teleconnections in the collapse and rebuilding of early Triassic marine ecosystems. *Palaeogeogr. Palaeoclimatol. Palaeoecol*. 308, 1–11. doi:10.1016/j.palaeo.2011.01.011

Algeo, T. J., Hinnov, L., Moser, J., Maynard, J. B., Elswick, E., Kuwahara, K., et al. (2010). Changes in productivity and redox conditions in the Panthalassic Ocean during the latest Permian. *Geology*. 38, 187–190. doi:10.1130/G30483.1

Algeo, T. J., Kuwahara, K., Sano, H., Bates, S., Lyons, T., Elswick, E., et al. (2011b). Spatial variation in sediment fluxes, redox conditions, and productivity in the Permian-Triassic Panthalassic Ocean. *Palaeogeogr. Palaeoclimatol. Palaeoecol*. 308, 65–83. doi:10.1016/j.palaeo.2010.07.007

Algeo, T. J., and Li, C. (2020). Redox classification and calibration of redox thresholds in sedimentary systems. *Geochem. Cosmochim. Acta*. 287, 8–26. doi:10.1016/j.gca.2020.01.055

Algeo, T. J., and Maynard, J. B. (2004). Trace-element behavior and redox facies in core shales of upper Pennsylvanian Kansas-type cyclothems. *Chem. Geol*. 206, 289–318. doi:10.1016/j.chemgeo.2003.12.009

Algeo, T. J., and Tribovillard, N. (2009). Environmental analysis of paleoceanographic systems based on molybdenum-uranium covariation. *Chem. Geol*. 268, 211–225. doi:10.1016/j.chemgeo.2009.09.001

Algeo, T. J., and Twitchett, R. J. (2010). Anomalous early Triassic sediment fluxes due to elevated weathering rates and their biological consequences. *Geology*. 38, 1023–1026. doi:10.1130/G31203.1

Anderson, R. F., Fleisher, M. Q., and Lao, Y. (2006). Glacial-interglacial variability in the delivery of dust to the central equatorial Pacific Ocean. *Earth Planet. Sci. Lett*. 242, 406–414. doi:10.1016/j.epsl.2005.11.061

Atkinson, A. C., Riani, M., and Cerioli, A. (2004). *Exploring multivariate data with the forward search*. New York, NY: Springer-Verlag.

Belzile, N., and Chen, Y.-W. (2017). Thallium in the environment: a critical review focused on natural waters, soils, sediments and airborne particles. *Appl. Geochem*. 84, 218–243. doi:10.1016/j.apgeochem.2017.06.013

Beveridge, N. A. S. (1994). "Evidence for a change in atmospheric circulation during the Younger Dryas," in *Long-term climatic variations*. Editors J.-C. Duplessy and M.-T. Spyridakis (Berlin, Germany: Springer-Verlag), 251–258. doi:10.1007/978-3-642-79066-9_10

Bishop, J. K. B. (1988). The barite-opal-organic carbon association in oceanic particulate matter. *Nature*. 332, 341–343. doi:10.1038/332341a0

Bond, D. P. G., Hilton, J., Wignall, P. B., Ali, J. R., Stevens, L. G., Sun, Y., et al. (2010). The middle Permian (Capitanian) mass extinction on land and in the oceans. *Earth-Sci. Rev*. 102, 100–116. doi:10.1016/j.earscirev.2010.07.004

Bottrell, S. H., and Newton, R. J. (2006). Reconstruction of changes in global sulfur cycling from marine sulfate isotopes. *Earth-Sci. Rev*. 75, 59–83. doi:10.1016/j.earscirev.2005.10.004

Boyle, E. A. (1983). Chemical accumulation variations under the Peru current during the past 130,000 years. *J. Geophys. Res. Oceans Atmos*. 88, 7667–7680. doi:10.1029/JC088iC12p07667

Brayard, A., Bucher, H., Escarguel, G., Fluteau, F., Bourquin, S., and Galfetti, T. (2006). The early Triassic ammonoid recovery: paleoclimatic significance of diversity gradients. *Palaeogeogr. Palaeoclimatol. Palaeoecol*. 239, 374–395. doi:10.1016/j.palaeo.2006.02.003

Brayard, A., Escarguel, G., Bucher, H., Monnet, C., Bruhwiler, T., Goudemand, N., et al. (2009). Good genes and good luck: ammonoid diversity and the end-Permian mass extinction. *Science*. 325, 1118–1121. doi:10.1126/science.1174638

Breit, G. N., and Wanty, R. B. (1991). Vanadium accumulation in carbonaceous rocks: a review of geochemical controls during deposition and diagenesis. *Chem. Geol*. 91, 83–97. doi:10.1016/0009-2541(91)90083-4

Brennecka, G. A., Herrmann, A. D., Algeo, T. J., and Anbar, A. D. (2011). Rapid expansion of oceanic anoxia immediately before the end-Permian mass extinction. *Proc. Natl. Acad. Sci. U.S.A*. 108, 17631–17634. doi:10.1073/pnas.1106039108

Brigatti, M. F., Galan, E., and Theng, B. K. G. (2006). "Chapter 2 structures and mineralogy of clay minerals," in *Handbook of clay science*. Editors F. Bergaya, B. K. G. Theng, and G. Lagaly (Amsterdam, Netherlands: Elsevier), 19–86. doi:10.1016/S1572-4352(05)01002-0

Burgess, S. D., and Bowring, S. A. (2015). High-precision geochronology confirms voluminous magmatism before, during, and after Earth's most severe extinction. *Sci. Adv*. 1, e1500470. doi:10.1126/sciadv.1500470

Burgess, S. D., Bowring, S., and Shen, S. Z. (2014). High-precision timeline for Earth's most severe extinction. *Proc. Natl. Acad. Sci. U. S. A*. 111, 3316–3321. doi:10.1073/pnas.1317692111

Burgess, S. D., Muirhead, J. D., and Bowring, S. A. (2017). Initial pulse of Siberian traps sills as the trigger of the end-Permian mass extinction. *Nat. Commun*. 8, 164. doi:10.1038/s41467-017-00083-9

Calvert, S. E., and Pedersen, T. F. (1993). Geochemistry of recent oxic and anoxic marine sediments: implications for the geological record. *Mar. Geol*. 113, 67–88. doi:10.1016/0025-3227(93)90150-T

Calvert, S. E., and Pedersen, T. F. (2007). "Chapter 14 Elemental proxies for palaeoclimatic and palaeoceanographic variability in marine sediments: interpretation and application," in *Developments in marine geology*. Editors C. Hillaire–Marcel and A. De Vernal (Amsterdam, Netherlands: Elsevier), 567–644. doi:10.1016/S1572-5480(07)01019-6

Cao, C. Q., Love, G. D., Hays, L. E., Wang, W., Shen, S. Z., and Summons, R. E. (2009). Biogeochemical evidence for euxinic oceans and ecological disturbance presaging the end-Permian mass extinction event. *Earth Planet. Sci. Lett*. 281, 188–201. doi:10.1016/j.epsl.2009.02.012

Cao, Y., Song, H., Algeo, T. J., Chu, D., Du, Y., Tian, L., et al. (2019). Intensified chemical weathering during the Permian-Triassic transition recorded in terrestrial and marine successions. *Palaeogeogr. Palaeoclimatol. Palaeoecol*. 519, 166–177. doi:10.1016/j.palaeo.2018.06.012

Chen, Z.-Q., and Benton, M. J. (2012). The timing and pattern of biotic recovery following the end-Permian mass extinction. *Nat. Geosci*. 5, 375–383. doi:10.1038/ngeo1475

Chen, B., Joachimski, M. M., Sun, Y., Shen, S., and Lai, X. (2011). Carbon and conodont apatite oxygen isotope records of Guadalupian–Lopingian boundary sections: climatic or sea-level signal? *Palaeogeogr. Palaeoclimatol. Palaeoecol*. 311, 145–153. doi:10.1016/j.palaeo.2011.08.016

Chen, B., Joachimski, M. M., Shen, S.-Z., Lambert, L. L., Lai, X.-L., Wang, X.-D., et al. (2013). Permian ice volume and palaeoclimate history: oxygen isotope proxies revisited. *Gondwana Res*. 24, 77–89. doi:10.1016/j.gr.2012.07.007

Chen, J., Algeo, T. J., Zhao, L., Chen, Z.-Q., Cao, L., Zhang, L., et al. (2015). Diagenetic uptake of rare earth elements by bioapatite, with an example from lower Triassic conodonts of south China. *Earth Sci. Rev*. 149, 181–202. doi:10.1016/j.earscirev.2015.01.013

Chen, J., Shen, S.-Z., Li, X.-H., Xu, Y.-G., Joachimski, M. M., Bowring, S. A., et al. (2016). High-resolution SIMS oxygen isotope analysis on conodont apatite from south China and implications for the end-Permian mass extinction. *Palaeogeogr. Palaeoclimatol. Palaeoecol*. 448, 26–38. doi:10.1016/j.palaeo.2015.11.025

Dehairs, F., Chesselet, R., and Jedwab, J. (1980). Discrete suspended particles of barite and the barium cycle in the open ocean. *Earth Planet. Sci. Lett*. 49, 528–550. doi:10.1016/0012-821X(80)90094-1

Dellwig, O., Leipe, T., März, C., Glockzin, M., Pollehne, F., Schnetger, B., et al. (2010). A new particulate Mn–Fe–P-shuttle at the redoxcline of anoxic basins. *Geochem. Cosmochim. Acta*. 74, 7100–7115. doi:10.1016/j.gca.2010.09.017

Duzgoren-Aydin, N. S., Aydin, A., and Malpas, J. (2002). Re-assessment of chemical weathering indices: case study on pyroclastic rocks of Hong Kong. *Eng. Geol*. 63, 99–119. doi:10.1016/S0013-7952(01)00073-4

Dymond, J., and Collier, R. (1996). Particulate barium fluxes and their relationships to biological productivity. *Deep-Sea Res. Pt. II*. 43, 1283–1308. doi:10.1016/0967-0645(96)00011-2

Elrick, M., Polyak, V., Algeo, T. J., Romaniello, S., Asmerom, Y., Herrmann, A. D., et al. (2017). Global-ocean redox variation during the middle-late Permian through early Triassic based on uranium isotope and Th/U trends of marine carbonates. *Geology*. 45, 163–166. doi:10.1130/G38585.1

Erickson, B. E., and Helz, G. R. (2000). Molybdenum(VI) speciation in sulfidic waters: stability and lability of thiomolybdates. *Geochem. Cosmochim. Acta*. 64, 1149–1158. doi:10.1016/S0016-7037(99)00423-8

Erwin, D. H. (1994). The Permo-Triassic extinction. *Nature*. 367, 231–236. doi:10.1038/367231a0

Feng, Q. L., and Algeo, T. J. (2014). Evolution of oceanic redox conditions during the Permo-Triassic transition: evidence from deepwater radiolarian facies. *Earth-Sci. Rev*. 137, 34–51. doi:10.1016/j.earscirev.2013.12.003

Fujisaki, W., Sawaki, Y., Matsui, Y., Yamamoto, S., Isozaki, Y., and Maruyama, S. (2019). Redox condition and nitrogen cycle in the Permian deep mid-ocean: a possible contrast between Panthalassa and Tethys. *Global Planet. Change*. 172, 179–199. doi:10.1016/j.gloplacha.2018.09.015

German, C. R., and Elderfield, H. (1990). Application of the Ce anomaly as a paleoredox indicator: the ground rules. *Paleoceanography*. 5, 823–833. doi:10.1029/PA005i005p00823

Golub, G. H., and Van Loan, C. F. (1989). *Matrix computations*. 2nd Edn. Baltimore, MD: Johns Hopkins University Press.

Grasby, S. E., Sanei, H., and Beauchamp, B. (2011). Catastrophic dispersion of coal fly ash into oceans during the latest Permian extinction. *Nat. Geosci*. 4, 104–107. doi:10.1038/ngeo1069

Grasby, S. E., Beauchamp, B., and Knies, J. (2016). Early Triassic productivity crises delayed recovery from world's worst mass extinction. *Geology*. 44, 779–782. doi:10.1130/G38141.1

Haq, B. U., and Schutter, S. R. (2008). A chronology of paleozoic sea-level changes. *Science*. 322, 64–68. doi:10.1126/science.1161648

Helz, G. R., Miller, C. V., Charnock, J. M., Mosselmans, J. F. W., Pattrick, R. A. D., Garner, C. D., et al. (1996). Mechanism of molybdenum removal from the sea and its concentration in black shales: EXAFS evidence. *Geochem. Cosmochim. Acta*. 60, 3631–3642. doi:10.1016/0016-7037(96)00195-0

Helz, G. R., Bura-Nakić, E., Mikac, N., and Ciglenečki, I. (2011). New model for molybdenum behavior in euxinic waters. *Chem. Geol*. 284, 323–332. doi:10.1016/j.chemgeo.2011.03.012

Hollis, C. J., Rodgers, K. A., Strong, C. P., Field, B. D., and Rogers, K. M. (2003). Paleoenvironmental changes across the Cretaceous/Tertiary boundary in the northern Clarence valley, southeastern Marlborough, New Zealand. *N. Z. J. Geol. Geophys*. 46, 209–234. doi:10.1080/00288306.2003.9515005

Holser, W. T. (1997). Evaluation of the application of rare-earth elements to paleoceanography. *Palaeogeogr. Palaeoclimatol. Palaeoecol*. 132, 309–323. doi:10.1016/S0031-0182(97)00069-2

Hori, R. S., Cho, C.-F., and Umeda, H. (1993). Origin of cyclicity in Triassic-Jurassic radiolarian bedded cherts of the Mino accretionary complex from Japan. *Isl. Arc*. 3, 170–180. doi:10.1111/j.1440-1738.1993.tb00084.x

Huerta-Diaz, M. A., and Morse, J. W. (1992). Pyritization of trace metals in anoxic marine sediments. *Geochem. Cosmochim. Acta*. 56, 2681–2702. doi:10.1016/0016-7037(92)90353-K

Ichiyama, Y., Ishiwatari, A., and Koizumi, K. (2008). Petrogenesis of greenstones from the Mino–Tamba belt, SW Japan: evidence for an accreted Permian Oceanic plateau. *Lithos*. 100, 127–146. doi:10.1016/j.lithos.2007.06.014

Isozaki, Y. (1994). "Superanoxia across the Permo–Triassic boundary: record in accreted deep-sea pelagic chert in Japan," in *Pangea: global Environments and resources*. Editors A. F. Embry, B. Beauchamp, and D. J. Glass (Calgary, Canada: Canadian Society of Petroleum Geologists, Memoir), 805–812.

Isozaki, Y. (1997). Permo-triassic boundary superanoxia and stratified superocean: records from lost deep sea. *Science*. 276, 235–238. doi:10.1126/science.276.5310.235

Isozaki, Y. (2009). Integrated "plume winter" scenario for the double-phased extinction during the Paleozoic–Mesozoic transition: the G-LB and P-TB events from a Panthalassan perspective. *J. Asian Earth Sci*. 36, 459–480. doi:10.1016/j.jseaes.2009.05.006

Isozaki, Y., Kawahata, H., and Minoshima, K. (2007a). The capitanian (permian) Kamura cooling event: the beginning of the Paleozoic–Mesozoic transition. *Palaeoworld*. 16, 16–30. doi:10.1016/j.palwor.2007.05.011

Isozaki, Y., Kawahata, H., and Ota, A. (2007b). A unique carbon isotope record across the Guadalupian–Lopingian (Middle–Upper Permian) boundary in mid-oceanic paleo-atoll carbonates: the high-productivity "Kamura event" and its collapse in Panthalassa. *Global Planet. Change*. 55, 21–38. doi:10.1016/j.gloplacha.2006.06.006

Isozaki, Y., Maruyama, S., Aoki, K., Nakama, T., Miyashita, A., and Otoh, S. (2010). Geotectonic subdivision of the Japanese islands revisited: categorization and definition of elements and boundaries of Pacific-type (Miyashiro-type) orogen. *J. Geogr*. 119, 999–1053. doi:10.5026/jgeography.119.999

Jenkyns, H. C. (2010). Geochemistry of oceanic anoxic events. *Geochem. Geophys. Geosyst*. 11, Q03004. doi:10.1029/2009GC002788

Jiang, H., Lai, X., Yan, C., Aldridge, R. J., Wignall, P., and Sun, Y. (2011). Revised conodont zonation and conodont evolution across the Permian–Triassic boundary at the Shangsi section, Guangyuan, Sichuan, South China. *Global Planet. Change*. 77, 103–115. doi:10.1016/j.gloplacha.2011.04.003

Jones, C. E., and Jenkyns, H. C. (2001). Seawater strontium isotopes, oceanic anoxic events, and seafloor hydrothermal activity in the Jurassic and Cretaceous. *Am. J. Sci*. 301, 112–149. doi:10.2475/ajs.301.2.112

Jones, G., Sano, H., and Valsami-Jones, E. (1993). Nature and tectonic setting of accreted basalts from the Mino terrane, central Japan. *J. Geol. Soc*. 150, 1167. doi:10.1144/gsjgs.150.6.1167

Kaiho, K., Saito, R., Ito, K., Miyaji, T., Biswas, R., Tian, L., et al. (2016). Effects of soil erosion and anoxic-euxinic ocean in the Permian-Triassic marine crisis. *Heliyon*. 2, e00137. doi:10.1016/j.heliyon.2016.e00137

Kajiwara, Y., Yamakita, S., Ishida, K., Ishiga, H., and Imai, A. (1994). Development of a largely anoxic stratified ocean and its temporary massive mixing at the

Permian/Triassic boundary supported by the sulfur isotopic record. *Palaeogeogr. Palaeoclimatol. Palaeoecol.* 111, 367–379. doi:10.1016/0031-0182(94)90072-8

Kakuwa, Y. (2008). Evaluation of palaeo-oxygenation of the ocean bottom across the Permian-Triassic boundary. *Global Planet. Change.* 63, 40–56. doi:10.1016/j.gloplacha.2008.05.002

Kato, Y., and Isozaki, Y. (2009). Comment on "evaluation of palaeo-oxygenation of the ocean bottom cross the Permian–Triassic boundary" by Kakuwa (2008): was the late Permian deep-superocean really oxic? *Global Planet. Change.* 69, 79–81. doi:10.1016/j.gloplacha.2009.01.003

Kato, Y., Nakao, K., and Isozaki, Y. (2002). Geochemistry of late Permian to early Triassic pelagic cherts from southwest Japan: implications for an oceanic redox change. *Chem. Geol.* 182, 15–34. doi:10.1016/S0009-2541(01)00273-X

Kearsey, T., Twitchett, R. J., Price, G. D., and Grimes, S. T. (2009). Isotope excursions and palaeotemperature estimates from the Permian/Triassic boundary in the Southern Alps (Italy). *Palaeogeogr. Palaeoclimatol. Palaeoecol.* 279, 29–40. doi:10.1016/j.palaeo.2009.04.015

Koschinsky, A., and Hein, J. R. (2003). Uptake of elements from seawater by ferromanganese crusts: solid-phase associations and seawater speciation. *Mar. Geol.* 198, 331–351. doi:10.1016/S0025-3227(03)00122-1

Kuwahara, K. (1997). Upper Permian radiolarian biostratigraphy: abundance zones of Albaillella. *News Osaka Micropaleont.* 10, 55–75.

Kuwahara, K., and Sano, H. (2017). Upper Guadalupian to lower lopingian latentifistularian (radiolaria) interval zones of the Mino belt in the Mt. Funabuseyama area, central Japan. *Paleontol. Res.* 21, 422–440. doi:10.2517/2017PR004

Kuwahara, K., Yao, A., and Yamakita, S. (1998). Reexamination of upper Permian radiolarian biostratigraphy. *Earth Sci.* 52, 391–404. doi:10.15080/agcjchikyukagaku.52.5_391

Langmuir, D. (1997). *Aqueous environmental geochemistry*. Upper Saddle River, NJ: Prentice-Hall.

Lau, K. V., Maher, K., Altiner, D., Kelley, B. M., Kump, L. R., Lehrmann, D. J., et al. (2016). Marine anoxia and delayed Earth system recovery after the end-Permian extinction. *Proc. Natl. Acad. Sci. U. S. A.* 113, 2360–2365. doi:10.1073/pnas.1515080113

Luo, G., Kump, L. R., Wang, Y., Tong, J., Arthur, M. A., Yang, H., et al. (2010). Isotopic evidence for an anomalously low oceanic sulfate concentration following end-Permian mass extinction. *Earth Planet. Sci. Lett.* 300, 101–111. doi:10.1016/j.epsl.2010.09.041

Maruoka, T., and Isozaki, Y. (2020). Sulfur and carbon isotopic systematics of Guadalupian-Lopingian (Permian) mid-Panthalassa: $\delta^{34}S$ and $\delta^{13}C$ profiles in accreted paleo-atoll carbonates in Japan. *Isl. Arc.* 29, e12362. doi:10.1111/iar.12362

McLennan, S. M. (1993). Weathering and global denudation. *J. Geol.* 101, 295–303

McLennan, S. M. (2001). Relationships between the trace element composition of sedimentary rocks and upper continental crust. *Geochem. Geophys. Geosyst.* 2, 2000GC000109. doi:10.1029/2000gc000109

Mcmanus, J., Berelson, W. M., Klinkhammer, G. P., Johnson, K. S., Coale, K. H., Anderson, R. F., et al. (1998). Geochemistry of barium in marine sediments: implications for its use as a paleoproxy. *Geochem. Cosmochim. Acta.* 62, 3453–3473. doi:10.1016/S0016-7037(98)00248-8

Morse, J. W., and Luther, G. W. (1999). Chemical influences on trace metal-sulfide interactions in anoxic sediments. *Geochem. Cosmochim. Acta.* 63, 3373–3378. doi:10.1016/S0016-7037(99)00258-6

Nesbitt, H. W., and Young, G. M. (1982). Early Proterozoic climates and plate motions inferred from major element chemistry of lutites. *Nature.* 299, 715–717. doi:10.1038/299715a0

Nesbitt, H. W., Young, G. M., Mclennan, S. M., and Keays, R. R. (1996). Effects of chemical weathering and sorting on the petrogenesis of siliciclastic sediments, with implications for provenance studies. *J. Geol.* 104, 525–542. doi:10.1086/629850

Nishikane, Y., Kaiho, K., Takahashi, S., Henderson, C. M., Suzuki, N., and Kanno, M. (2011). The Guadalupian-Lopingian boundary (Permian) in a pelagic sequence from Panthalassa recognized by integrated conodont and radiolarian biostratigraphy. *Mar. Micropaleontol.* 78, 84–95. doi:10.1016/j.marmicro.2010.10.002

Nishikane, Y., Kaiho, K., Henderson, C. M., Takahashi, S., and Suzuki, N. (2014). Guadalupian–Lopingian conodont and carbon isotope stratigraphies of a deep chert sequence in Japan. *Palaeogeogr. Palaeoclimatol. Palaeoecol.* 403, 16–29. doi:10.1016/j.palaeo.2014.02.033

Nürnberg, C. C., Bohrmann, G., Schlüter, M., and Frank, M. (1997). Barium accumulation in the atlantic sector of the southern ocean: results from 190,000-year records. *Paleoceanography.* 12, 594–603. doi:10.1029/97PA01130

Ohta, T., and Arai, H. (2007). Statistical empirical index of chemical weathering in igneous rocks: a new tool for evaluating the degree of weathering. *Chem. Geol.* 240, 280–297. doi:10.1016/j.chemgeo.2007.02.017

Ohta, J., Yasukawa, K., Nozaki, T., Takaya, Y., Mimura, K., Fujinaga, K., et al. (2020). Fish proliferation and rare-Earth deposition by topographically induced upwelling at the late Eocene cooling event. *Sci. Rep.* 10, 9896. doi:10.1038/s41598-020-66835-8

Onoue, T., Takahata, N., Miura, M., Sato, H., Ishikawa, A., Soda, K., et al. (2019). Enhanced flux of extraterrestrial 3 He across the Permian–Triassic boundary. *Prog. Earth Planet. Sci.* 6, 18. doi:10.1186/s40645-019-0267-0

Parker, A. (1970). An index of weathering for silicate rocks. *Geol. Mag.* 107, 501–504. doi:10.1017/S0016756800058581

Payne, J. L., and Clapham, M. E. (2012). End-permian mass extinction in the oceans: an ancient analog for the Twenty-first century? *Annu. Rev. Earth Planet. Sci.* 40, 89–111. doi:10.1146/annurev-earth-042711-105329

Pirajno, F. (2009). *Hydrothermal processes and mineral systems*. Dordrecht, Netherlands: Springer Netherlands.

Pogge Von Strandmann, P. A. E., Jenkyns, H. C., and Woodfine, R. G. (2013). Lithium isotope evidence for enhanced weathering during Oceanic anoxic event 2. *Nat. Geosci.* 6, 668–672. doi:10.1038/ngeo1875

Price, J. R., and Velbel, M. A. (2003). Chemical weathering indices applied to weathering profiles developed on heterogeneous felsic metamorphic parent rocks. *Chem. Geol.* 202, 397–416. doi:10.1016/j.chemgeo.2002.11.001

Railsback, L. B. (2007). Patterns in the compositions of oxysalt and sulfosalt minerals, and the paradoxical nature of quartz. *Am. Mineral.* 92, 356–369. doi:10.2138/am.2007.2310

Rea, D. K. (1994). The paleoclimatic record provided by eolian deposition in the deep sea: the geologic history of wind. *Rev. Geophys.* 32, 159–195. doi:10.1029/93RG03257

Rea, D. K., Leinen, M., and Janecek, T. R. (1985). Geologic approach to the long-term history of atmospheric circulation. *Science.* 227, 721–725. doi:10.1126/science.227.4688.721

Rehkämper, M., and Nielsen, S. G. (2004). The mass balance of dissolved thallium in the oceans. *Mar. Chem.* 85, 125–139. doi:10.1016/j.marchem.2003.09.006

Reyment, R. A., and Hirano, H. (1999). Exploratory multivariate statistical analysis of geochemical data from the Cenomanian–Turonian transition of the Yezo Supergroup, Hokkaido, Japan. *Cretac. Res.* 20, 539–546. doi:10.1006/cres.1999.0165

Reynard, B., Lécuyer, C., and Grandjean, P. (1999). Crystal-chemical controls on rare-earth element concentrations in fossil biogenic apatites and implications for paleoenvironmental reconstructions. *Chem. Geol.* 155, 233–241. doi:10.1016/S0009-2541(98)00169-7

Sadiq, M. (1988). Thermodynamic solubility relationships of inorganic vanadium in the marine environment. *Mar. Chem.* 23, 87–96. doi:10.1016/0304-4203(88)90024-2

Safonova, I., Maruyama, S., Kojima, S., Komiya, T., Krivonogov, S., and Koshida, K. (2016). Recognizing OIB and MORB in accretionary complexes: a new approach based on ocean plate stratigraphy, petrology and geochemistry. *Gondwana Res.* 33, 92–114. doi:10.1016/j.gr.2015.06.013

Sano, H. (1988a). Permian oceanic-rocks of Mino terrane, central Japan., Part I. Cert facies. *J. Geol. Soc. Japan.* 94, 697–709. doi:10.5575/geosoc.94.697

Sano, H. (1988b). Permian oceanic-rocks of Mino terrane, central Japan Part II. Limestone facies. *J. Geol. Soc. Japan.* 94, 963–976. doi:10.5575/geosoc.94.963

Sano, H. (1989). Permian oceanic-rocks of Mino terrane, central Japan. Part III. Limestone-breccia facies. *J. Geol. Soc. Japan.* 95, 527–540. doi:10.5575/geosoc.95.527

Sano, H. (2018). Stratigraphy and age of the Permian to Triassic chert-dominant succession of the Mino Belt in the eastern part of the Funabuseyama rock mass, western Gifu prefecture. *J. Geol. Soc. Japan.* 124, 449–467. doi:10.5575/geosoc.2018.0010

Sano, H., Yamagata, T., and Horibo, K. (1992). Tectonostratigraphy of Mino terrane: Jurassic accretionary complex of southwest Japan. *Palaeogeogr. Palaeoclimatol. Palaeoecol.* 96, 41–57. doi:10.1016/0031-0182(92)90058-D

Sano, H., Kuwahara, K., Yao, A., and Agematsu, S. (2010). Panthalassan seamount-associated Permian-Triassic boundary siliceous rocks, Mino Terrane, central Japan. *Paleontol. Res.* 14, 293–314. doi:10.2517/1342-8144-14.4.293

Sano, H., Kuwahara, K., Yao, A., and Agematsu, S. (2012a). Stratigraphy and age of the Permian-Triassic boundary siliceous rocks of the Mino terrane in the Mt. Funabuseyama area, central Japan. *Paleontol. Res.* 16, 124–145. doi:10.2517/1342-8144-16.2.124

Sano, H., Wada, T., and Naraoka, H. (2012b). Late Permian to early Triassic environmental changes in the Panthalassic ocean: record from the seamount-associated deep-marine siliceous rocks, central Japan. *Palaeogeogr. Palaeoclimatol. Palaeoecol.* 363, 1–10. doi:10.1016/j.palaeo.2012.07.018

Sato, H., Takaya, Y., Yasukawa, K., Fujinaga, K., Onoue, T., and Kato, Y. (2020). Biotic and environmental changes in the Panthalassa Ocean across the Norian (late Triassic) impact event. *Prog. Earth Planet. Sci.* 7, 61. doi:10.1186/s40645-020-00371-x

Schmitz, B. (1987). The TiO_2/Al_2O_3 ratio in the Cenozoic Bengal abyssal fan sediments and its use as a paleostream energy indicator. *Mar. Geol.* 76, 195–206. doi:10.1016/0025-3227(87)90029-6

Schobben, M., Stebbins, A., Ghaderi, A., Strauss, H., Korn, D., and Korte, C. (2015). Flourishing ocean drives the end-Permian marine mass extinction. *Proc. Natl. Acad. Sci. U. S. A.* 112, 10298–10303. doi:10.1073/pnas.1503755112

Schobben, M., Foster, W., Sleveland, A. R. N., Zuchuat, V., Svensen, H., Planke, S., et al. (2020). A nutrient control on marine anoxia during the end-Permian mass extinction. *Nat. Geosci.* 13, 640–646. doi:10.1038/s41561-020-0622-1

Schoepfer, S. D., Henderson, C. M., Garrison, G. H., Foriel, J., Ward, P. D., Selby, D., et al. (2013). Termination of a continent-margin upwelling system at the Permian–Triassic boundary (Opal Creek, Alberta, Canada). *Global Planet. Change.* 105, 21–35. doi:10.1016/j.gloplacha.2012.07.005

Scholz, F., Mcmanus, J., and Sommer, S. (2013). The manganese and iron shuttle in a modern euxinic basin and implications for molybdenum cycling at euxinic ocean margins. *Chem. Geol.* 355, 56–68. doi:10.1016/j.chemgeo.2013.07.006

Schroeder, J. O., Murray, R. W., Leinen, M., Pflaum, R. C., and Janecek, T. R. (1997). Barium in equatorial Pacific carbonate sediment: terrigenous, oxide, and biogenic associations. *Paleoceanography.* 12, 125–146. doi:10.1029/96PA02736

Sephton, M., Looy, C., Brinkhuis, H., Wignall, P., De Leeuw, J., and Visscher, H. (2005). Catastrophic soil erosion during the end-Permian biotic crisis. *Geology.* 33, 941–944. doi:10.1130/G21784.1

Shaffer, G. (1986). Phosphate pumps and shuttles in the black sea. *Nature.* 321, 515–517. doi:10.1038/321515a0

Sheldon, N. D. (2006). Abrupt chemical weathering increase across the Permian–Triassic boundary. *Palaeogeogr. Palaeoclimatol. Palaeoecol.* 231, 315–321. doi:10.1016/j.palaeo.2005.09.001

Sheldon, N. D., and Tabor, N. J. (2009). Quantitative paleoenvironmental and paleoclimatic reconstruction using paleosols. *Earth-Sci. Rev.* 95, 1–52. doi:10.1016/j.earscirev.2009.03.004

Shen, J., Chen, J., Algeo, T. J., Yuan, S., Feng, Q., Yu, J., et al. (2019). Evidence for a prolonged Permian-Triassic extinction interval from global marine mercury records. *Nat. Commun.* 10, 1563. doi:10.1038/s41467-019-09620-0

Shimmield, G. B., and Mowbray, S. R. (1991). The inorganic geochemical record of the Northwest Arabian Sea: a history of productivity variation over the last 400 k.y. from sites 722 and 724. *Proc. Ocean Drill. Progr. Sci. Results.* 117, 409–429. doi:10.2973/ODP.PROC.SR.117.170.1991

Sholkovitz, E. R., Landing, W. M., and Lewis, B. L. (1994). Ocean particle chemistry: the fractionation of rare earth elements between suspended particles and seawater. *Geochem. Cosmochim. Acta.* 58, 1567–1579. doi:10.1016/0016-7037(94)90559-2

Soda, K., and Onoue, T. (2018). Paleoenvironmental reconstruction for termination stage of Superanoxia in Middle Triassic (Anisian) sedimentary sequence of the Mino belt, central Japan. *Isl. Arc.* 27, e12262. doi:10.1111/iar.12262

Soda, K., and Onoue, T. (2019). Multivariate analysis of geochemical compositions of bedded chert during the Middle Triassic (Anisian) oceanic anoxic events in the Panthalassic Ocean. *Geochem. J.* 53, 91–102. doi:10.2343/geochemj.2.0540

Stanley, S. M. (2016). Estimates of the magnitudes of major marine mass extinctions in earth history. *Proc. Natl. Acad. Sci. U. S. A.* 113, E6325–E6334. doi:10.1073/pnas.1613094113

Stumm, W., and Morgan, J. J. (1996). *Aquatic chemistry: chemical equilibria and rates in natural waters.* 3rd Edn. Hoboken, NJ: Wiley.

Sugitani, K., Sano, H., Adachi, M., and Sugisaki, R. (1991). Permian hydrothermal deposits in the Mino Terrane, central Japan: implications for hydrothermal plumes in an ancient ocean Basin. *Sediment. Geol.* 71, 59–71. doi:10.1016/0037-0738(91)90007-Z

Sun, Y. D., Joachimski, M. M., Wignall, P. B., Yan, C. B., Chen, Y. L., Jiang, H. S., et al. (2012). Lethally hot temperatures during the Early Triassic greenhouse. *Science.* 338, 366–370. doi:10.1126/science.1224126

Sun, H., Xiao, Y., Gao, Y., Zhang, G., Casey, J. F., and Shen, Y. (2018). Rapid enhancement of chemical weathering recorded by extremely light seawater lithium isotopes at the Permian-Triassic boundary. *Proc. Natl. Acad. Sci. U. S. A.* 115, 3782–3787. doi:10.1073/pnas.1711862115

Suzuki, N., Ishida, K., Shinomiya, Y., and Ishiga, H. (1998). High productivity in the earliest Triassic ocean: black shales, Southwest Japan. *Palaeogeogr. Palaeoclimatol. Palaeoecol.* 141, 53–65. doi:10.1016/S0031-0182(98)00009-1

Takahashi, S., Yamasaki, S., Ogawa, Y., Kimura, K., Kaiho, K., Yoshida, T., et al. (2014). Bioessential element-depleted ocean following the euxinic maximum of the end-Permian mass extinction. *Earth Planet. Sci. Lett.* 393, 94–104. doi:10.1016/j.epsl.2014.02.041

Takahashi, S., Nakada, R., Watanabe, Y., and Takahashi, Y. (2019). Iron-depleted pelagic water at the end-Permian mass extinction inferred from chemical species of iron and molybdenum in deep-sea sedimentary rocks. *Palaeogeogr. Palaeoclimatol. Palaeoecol.* 516, 384–399. doi:10.1016/j.palaeo.2018.12.014

Takahata, N., Onoue, T., Sano, Y., and Isozaki, Y. (2019). A significantly high He isotopic signature from the end-Paleozoic (250 Ma) extinction-related interval: for detecting ancient extraterrestrial fluxes through the Earth's history since the Hadean. *J. Geogr.* 128, 667–679. doi:10.5026/jgeography.128.667

Takiguchi, T., Sugitani, K., Yamamoto, K., and Suzuki, K. (2006). Biogeochemical signatures preserved in ancient siliceous sediments; new perspectives to Triassic radiolarian bedded chert compositions. *Geochem. J.* 40, 33–45. doi:10.2343/geochemj.40.33

Taylor, S. R., and Mclennan, S. M. (1985). *The continental crust: its composition and evolution.* Oxford, United Kingdom: Blackwell.

Tribovillard, N., Algeo, T. J., Lyons, T., and Riboulleau, A. (2006). Trace metals as paleoredox and paleoproductivity proxies: an update. *Chem. Geol.* 232, 12–32. doi:10.1016/j.chemgeo.2006.02.012

Tribovillard, N., Algeo, T. J., Baudin, F., and Riboulleau, A. (2012). Analysis of marine environmental conditions based on molybdenum-uranium covariation-applications to Mesozoic paleoceanography. *Chem. Geol.* 324, 46–58. doi:10.1016/j.chemgeo.2011.09.009

Turner, B. F., Stallard, R. F., and Brantley, S. L. (2003). Investigation of *in situ* weathering of quartz diorite bedrock in the Rio Lcacos Basin, Luquillo Experimental Forest, Puerto Rico. *Chem. Geol.* 202, 313–341. doi:10.1016/j.chemgeo.2003.05.001

Tyson, R., and Pearson, T. (1991). Modern and ancient continental shelf anoxia: an overview. *Geol. Soc. Sepc. Publ.* 58, 1–24. doi:10.1144/GSL.SP.1991.058.01.01

Van Huffel, S., and Vanderwalle, J. (1991). *The total least squares problem: computational aspects and analysis.* University City, Philadelphia: Philadelphia Society for Industrial and Applied Mathematics.

Wakita, K. (1988). Origin of chaotically mixed rock bodies in the early Jurassic to early cretaceous sedimentary complex of the Mino terrane, central Japan. *Bull. Geol. Surv. Jpn.* 39, 675–757.

Wakita, K., Harayama, K., Kano, K., Mimura, K., and Sakamoto, T. (1992). *Geological Map of Japan 1:200,000, Gifu.* Tsukuba, Japan: Geological Survey of Japan.

Wanty, R. B., and Goldhaber, M. B. (1992). Thermodynamics and kinetics of reactions involving vanadium in natural systems: accumulation of vanadium in sedimentary rocks. *Geochem. Cosmochim. Acta.* 56, 1471–1483. doi:10.1016/0016-7037(92)90217-7

Wignall, P. B. (2007). The End-Permian mass extinction—how bad did it get? *Geobiology.* 5, 303–309. doi:10.1111/j.1472-4669.2007.00130.x

Wignall, P. B., and Twitchett, R. J. (1996). Oceanic anoxia and the end Permian mass extinction. *Science.* 272, 1155–1158. doi:10.1126/science.272.5265.1155

Wignall, P. B., Sun, Y., Bond, D. P. G., Izon, G., Newton, R. J., Védrine, S., et al. (2009). Volcanism, mass extinction, and carbon isotope fluctuations in the

Middle Permian of China. *Science*. 324, 1179–1182. doi:10.1126/science.1171956

Wignall, P. B., Bond, D. P. G., Kuwahara, K., Kakuwa, Y., Newton, R. J., and Poulton, S. W. (2010). An 80 million year oceanic redox history from Permian to Jurassic pelagic sediments of the Mino-Tamba terrane, SW Japan, and the origin of four mass extinctions. *Global Planet. Change*. 71, 109–123. doi:10.1016/j.gloplacha.2010.01.022

Woronow, A., and Love, K. M. (1990). Quantifying and testing differences among Means of compositional data suites. *Math. Geol*. 22, 837–852. doi:10.1007/Bf00890666

Yang, J., Cawood, P. A., Du, Y., Li, W., and Yan, J. (2016). Reconstructing Early Permian tropical climates from chemical weathering indices. *Geol. Soc. Am. Bull*. 128, 739–751. doi:10.1130/B31371.1

Yao, W., and Millero, F. J. (1996). Oxidation of hydrogen sulfide by hydrous Fe(III) oxides in seawater. *Mar. Chem*. 52, 1–16. doi:10.1016/0304-4203(95)00072-0

Yao, J., Yao, A., and Kuwahara, K. (2001). Upper Permian biostratigraphic correlation between conodont and radiolarian zones in the Tamba-Mino terrane, Southwest Japan. *J. Geosci. Osaka City Univ*. 44, 97–119.

Zachos, J. C., Arthur, M. A., and Dean, W. E. (1989). Geochemical evidence for suppression of pelagic marine productivity at the Cretaceous/Tertiary boundary. *Nature*. 337, 61–64. doi:10.1038/337061a0

Zhang, L., Algeo, T. J., Cao, L., Zhao, L., Chen, Z.-Q., and Li, Z. (2016). Diagenetic uptake of rare earth elements by conodont apatite. *Palaeogeogr. Palaeoclimatol. Palaeoecol*. 458, 176–197. doi:10.1016/j.palaeo.2015.10.049

Zhang, G., Zhang, X., Hu, D., Li, D., Algeo, T. J., Farquhar, J., et al. (2017). Redox chemistry changes in the Panthalassic Ocean linked to the end-Permian mass extinction and delayed Early Triassic biotic recovery. *Proc. Natl. Acad. Sci. U. S. A*. 114, 1806–1810. doi:10.1073/pnas.1610931114

Zhang, F., Algeo, T. J., Romaniello, S. J., Cui, Y., Zhao, L., Chen, Z.-Q., et al. (2018a). Congruent Permian-Triassic $\delta^{238}U$ records at Panthalassic and Tethyan sites: confirmation of global-oceanic anoxia and validation of the U-isotope paleoredox proxy. *Geology*. 46, 327–330. doi:10.1130/G39695.1

Zhang, F., Romaniello, S. J., Algeo, T. J., Lau, K. V., Clapham, M. E., Richoz, S., et al. (2018b). Multiple episodes of extensive marine anoxia linked to global warming and continental weathering following the latest Permian mass extinction. *Sci. Adv*. 4, e1602921. doi:10.1126/sciadv.1602921

Zhang, B., Yao, S., Hu, W., Ding, H., Liu, B., and Ren, Y. (2019). Development of a high-productivity and anoxic-euxinic condition during the late Guadalupian in the Lower Yangtze region: implications for the mid-Capitanian extinction event. *Palaeogeogr. Palaeoclimatol. Palaeoecol*. 531, 108630. doi:10.1016/j.palaeo.2018.01.021

Zhang, F., Shen, S.-Z., Cui, Y., Lenton, T. M., Dahl, T. W., Zhang, H., et al. (2020). Two distinct episodes of marine anoxia during the Permian-Triassic crisis evidenced by uranium isotopes in marine dolostones. *Geochem. Cosmochim. Acta*. 287, 165–179. doi:10.1016/j.gca.2020.01.032

Zheng, Y., Anderson, R. F., Van Geen, A., and Kuwabara, J. (2000). Authigenic molybdenum formation in marine sediments: a link to pore water sulfide in the Santa Barbara Basin. *Geochem. Cosmochim. Acta*. 64, 4165–4178. doi:10.1016/S0016-7037(00)00495-6

Conflict of Interest: The authors declare that the research was conducted in the absence of any commercial or financial relationships that could be construed as a potential conflict of interest.